AGU PUBLICATIONS

JGR

Journal of Geophysical Research: Earth Surface

RESEARCH ARTICLE
10.1002/2017JF004282

Key Points:
- We combine (U-Th)/He dating and cosmogenic ^{3}He measurements in supergene iron oxides to study relic banded iron-formation (BIF) landscapes
- We confirm that cangas are long-lasting features that armor the landscape and slow the delivery of weathered BIF to erosion
- Precipitation of goethite cements takes place primarily in the subsurface

Correspondence to:
H. S. Monteiro,
hevelynbr@gmail.com

Citation:
Monteiro, H. S., Vasconcelos, P. M. P., & Farley, K. A. (2018). A combined (U-Th)/He and cosmogenic ^{3}He record of landscape armoring by biogeochemical iron cycling. *Journal of Geophysical Research: Earth Surface*, *123*, 298–323. https://doi.org/10.1002/2017JF004282

Received 8 MAR 2017
Accepted 5 DEC 2017
Accepted article online 29 JAN 2018
Published online 20 FEB 2018

A Combined (U-Th)/He and Cosmogenic ^{3}He Record of Landscape Armoring by Biogeochemical Iron Cycling

H. S. Monteiro[1], P. M. P. Vasconcelos[1,2], and K. A. Farley[2]

[1]School of Earth and Environmental Sciences, University of Queensland, Brisbane, Queensland, Australia, [2]Division of Geological and Planetary Sciences, California Institute of Technology, Pasadena, CA, USA

Abstract (U-Th)/He geochronology and cosmogenic ^{3}He in iron oxides reveal mineral precipitation ages as old as 55 Ma and exposure ages greater than 5 Ma for canga-cemented plateaus in the Quadrilátero Ferrífero, Brazil, showing that lateritic profiles overlying banded iron-formation (BIF) landscapes in tropical regions have a long history of surface exposure. The long-term erosion history obtained from cosmogenic ^{3}He on BIF plateaus confirms that relic surfaces persist in the landscape for millions of years. Combined ^{3}He and (U-Th)/He dating shows that cangas are preferentially goethite cemented by biogeochemical reactions in the subsurface. Importantly, pebbles of hematite-magnetite in colluvia or shallow creeks draining the canga-cemented plateaus record a much longer exposure history than in situ canga blocks, showing that even older duricrusts, now eroded, once blanketed these plateaus. Physically stable but biogeochemically dynamic, cangas armor the landscape by pervasive and recurrent iron cycling and cementation, slowing down the delivery of weathered BIF or friable hematite–magnetite ore to erosion.

1. Introduction

In geomorphology, weathering is often portrayed as the combination of physical, chemical, and biological processes that turn bedrock into erodible material (e.g., Braun et al., 2016; Tucker & Hancock, 2010; Tucker & Singerland, 1994). The rate of delivery of this erodible material to drainage systems ultimately controls landscape evolution (Carson & Kirkby, 1972). In fast evolving landscapes, the weathered blanket is quickly eroded, and this effective transfer of physical and chemical sediments to the drainage system is particularly pronounced in active tectonic environments (e.g., Himalaya, Vance et al., 2003; San Gabriel Mountains, CA, DiBiase et al., 2010, and references therein). The role of chemical and physical weathering in shielding landscapes against erosion is less well-appreciated.

Canga, an iron duricrust that caps weathered banded iron-formations (BIFs), is essentially a shallow karstic breccia derived from significant mass loss during BIF weathering. This breccia is shaped by biologically and gravity-driven mechanical processes that allow material to move vertically up-and-down within the canga profile. In addition, biologically driven mineral dissolution-reprecipitation allows the brecciated material to be recemented repeatedly through time (Monteiro et al., 2014). Field inferences (King, 1956; Twidale, 1956), ^{40}Ar/^{39}Ar geochronology (Carmo & Vasconcelos, 2004; Spier et al., 2006; Vasconcelos et al., 1994), and (U-Th)/He geochronology (Monteiro et al., 2014; Shuster et al., 2005, 2012) show that cangas blanketing weathered BIFs in cratonic landscapes constitute some of the longest-lived continuously exposed land surfaces on Earth. The chemical and physical weathering processes that form these duricrusts may impede erosion instead of helping the delivery of disaggregated bedrock to the drainage system (Vasconcelos, 1999). If true, physical and chemical weathering may function in exactly the opposite way as portrayed in physical landscape models (e.g., Tucker & Hancock, 2010; Tucker & Singerland, 1994). Therefore, understanding this moderating effect of weathering in sediment production is essential in quantifying and modeling landscape evolution in cratonic environments.

Cosmogenic ^{3}He concentrations generated by spallation reactions on Fe and O in Fe-oxyhydroxides and (U-Th)/He precipitation ages (*pAs*) for those minerals may help to unravel the role of supergene iron cycling in slowing down erosion and armoring landscapes (Monteiro et al., 2014; Shuster et al., 2012). For example, (U-Th)/He *pAs* for supergene goethite cementing cangas at Carajás, Pará, and the Quadrilátero Ferrífero (QF), Minas Gerais, Brazil, reveal that duricrusts began forming some time before ~60 Ma (Monteiro et al., 2014;

Shuster et al., 2005, 2012). Canga longevity is independently confirmed by cosmogenic isotope results (Fujioka et al., 2010; Shuster et al., 2012). At Carajás, cosmogenic ^{3}He concentrations in hypogene hematite fragments and associated supergene goethite cements show that canga-blanketed surfaces erode very slowly (0.13–0.46 m.Ma^{-1}) over tens of millions of years (Shuster et al., 2012). Cosmogenic ^{53}Mn concentrations in these iron oxides also suggest a long exposure history under very low rates of erosion (Fujioka et al., 2010).

These previous (U-Th)/He and cosmogenic isotope results confirm the longevity of iron duricrusts, but they do not provide information on the mechanisms linking the advance of weathering fronts at depth to the delivery of clastic material to the drainage system at the surface. Measuring both (U-Th)/He ages and cosmogenic ^{3}He concentrations is a powerful way of determining when, where (surface versus subsurface), and how goethite cementation takes place. This information permits resolving age, depth of precipitation, and history of shallow burial and exhumation of goethite cements, improving our understanding of the processes controlling canga evolution and armoring of landscapes.

In this study, we measure concentrations of cosmogenic ^{3}He in supergene goethite cements, in hematite-magnetite clasts embedded in duricrusts, and in hematite-magnetite ± goethite pebbles eroded from canga-armored plateaus at Serras da Moeda, Serrinhas, and Gandarela, Quadrilátero Ferrífero, Minas Gerais, Brazil (Figure 1). We also combine previously determined *pAs* for goethite veins in saprolites, fragments of goethite veins cemented into cangas, and goethite cementing the cangas (n = 157) with new ages for additional cements (n = 138). The combined (U-Th)/He and cosmogenic ^{3}He methods reveal a history of BIF partial dissolution, fragmentation, translocation, local transport, re-cementation, possible shallow reburial and reexhumation, and very slow physical erosion by surface degradation and scarp retreat.

2. Geology and Geomorphology of the Quadrilátero Ferrífero

The Quadrilátero Ferrífero (QF), an ~7,000 km^{2} region within the São Francisco craton, southeastern Brazil, comprises deeply weathered Archean and Proterozoic metavolcanics, metapelites, metaconglomerates, quartzites, BIFs, and carbonates (Alkmim & Marshak, 1998). Paleoproterozoic (*Transamazonian)* and Neoproterozoic to Cambrian (*Brasiliano)* tectonism (Chemale et al., 1994) promoted magmatism, greenschist to amphibolite grade metamorphism, and deformation of the supracrustal rocks into large-scale synclines and anticlines (Dorr, 1969). Tectonic activity after ~500 Ma is only detectable by thermochronology (Carmo et al., 2004) or surficial features (e.g., abrupt changes in drainage profiles) (Magalhães & Saadi, 1994), suggesting that this is a relatively stable part of the São Francisco craton. Apatite fission track thermochronology reveals that regional exhumation started at ~180 Ma, before the opening of the Atlantic Ocean (Carmo et al., 2004; Kohn et al., 2016).

Geomorphologically, the QF is bounded by elevated quartzite and BIF plateaus and ridges (Caraça, Gandarela, Moeda, Curral, Serrinhas, and Ouro Branco) ranging from 2,100 to 1,100 m, incised by steep valleys and surrounded by lower elevation (500–800 m) convex hills (the "Mar de Morros" or "Sea of Hills" of Ab'Saber, 1966) (Figure 1a). The highest elevations in the QF are underlain by quartzites on the eastern margin (Serra do Caraça), but we focus our investigation on plateaus and ridges formed primarily on BIFs in the central and western (Gandarela, Moeda, and Serrinhas) parts of the QF (Figure 1). Modern drainage in the QF (e.g., Rio das Velhas) preferentially incises into schists, phyllites, granites, and gneisses, while granitic-gneissic units underlay the surrounding "Mar de Morros" landscape (Figure 1a).

Climate in the QF is humid subtropical (ranging from Cwa to Cwb in Köppen-Geiger's classification) with annual rainfall between 1,300 and 1,600 mm (Alvares et al., 2013), a wet season from November to April, and a dry season from May to October. All rivers in the region are perennial, except for small creeks draining the highest-elevation plateaus, which are intermittent and flow torrentially only during and immediately after summer storms. Water analysis for a natural spring ("Nascente da Mina") at the Pico Mine (Serra das Serrinhas, Figure 1) shows neutral (pH = 7.12), moderate salinity (TDS = 197 mg.L^{-1}), low dissolved oxygen (3.7 mg.L^{-1}), Ca- and Mg-rich (78 and 20 mg.L^{-1}, respectively), and bicarbonate-buffered (68.9 mg.L^{-1}) waters devoid of dissolved Fe ($<$0.01 mg.L^{-1}). Vegetation ranges from tropical to subtropical rainforest in most of the region, except areas underlain by iron duricrusts or deeply weathered quartzites, which host endemic epilithic ("rupestre") vegetation (Jacobi et al., 2007).

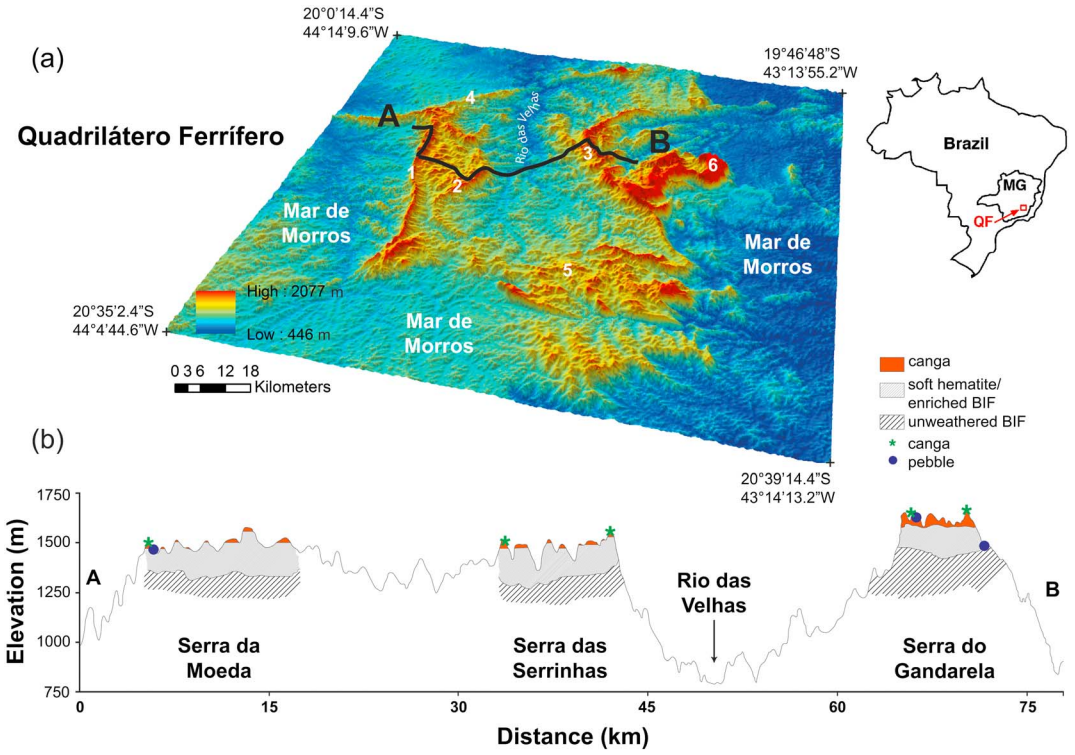

Figure 1. The (a) digital elevation model and (b) topographic cross section (A-B) depicts the BIF landscape and shows the most prominent regional landscape features (1 = Serra da Moeda; 2 = Serra das Serrinhas; 3 = Serra do Gandarela; 4 = Serra do Curral; 5 = Serra do Ouro Branco; and 6 = Serra do Caraça) in the Quadrilátero Ferrífero (QF) and adjacent regions, Minas Gerais, Brazil. The interior of the QF is dissected by the das Velhas River and its tributaries, and low-elevation convex hills dominate the surrounding "Mar de Morros" landscape. Schematic and simplified geological cross sections (Carlos et al., 2014; Spier et al., 2006, 2008, 2003) plotted on the topographic profile illustrate that weathering profiles as deep as 250 m are capped by continuous or intermittent cangas. The approximate location of cangas and hematite–magnetite pebbles investigated in this study is shown.

$^{40}Ar/^{39}Ar$ ages obtained for the deeply weathered profiles in the QF (Carmo & Vasconcelos, 2004; Spier et al., 2006) suggest a surface exposure and weathering history already ongoing by the end of the Cretaceous (~70 Ma). These ancient weathering profiles are overlain by Fe duricrusts, which probably began armoring the landscape with the onset of weathering (Monteiro et al., 2014; Shuster et al., 2012). Depth and lateral continuity of the duricrusts vary across the region, where the highest-elevation plateaus are capped by the deepest (up to 70 m according to Carlos et al., 2014) and most continuous canga blankets (e.g., Serra do Gandarela, Figure 1b) (Baltazar et al., 2005a). Low-elevation plateaus are overlain by intermittent and shallower cangas (up to 30 m) (e.g., Serra da Moeda, Figure 1b) (Baltazar et al., 2005b, 2005c), whereas the narrowest and mostly discontinuous ridges are blanketed by intermittent cangas (e.g., Serra das Serrinhas, Figure 1b) (Baltazar et al., 2005b, 2005c). Rills incised into plateaus and carving their shoulders contain transported fragments of eroded duricrusts (Figures 2a–2e). Saddles between plateaus contain colluvia hosting fragments of ancient duricrusts that were eroded, transported to lower parts of the landscape, and recemented (Figure 2f).

3. Methods

Fragments of canga and hematite-magnetite ± goethite clasts and pebbles were collected at the surface from eight pristine sites, unaffected by mining, along the Serras da Moeda, Serrinhas, and Gandarela (Figures 1–3). Goethite veins were collected from mine sites or roadcuts exposing saprolites at lower elevations (Figure 3f). Canga blocks and goethite and hematite-magnetite ± goethite pebbles were collected in situ and from colluvia, transported cangas, or shallow channels draining the plateaus (Figures 1–3). In order to test the reproducibility of results for duplicate samples and to test the distribution of cosmogenic ^{3}He with

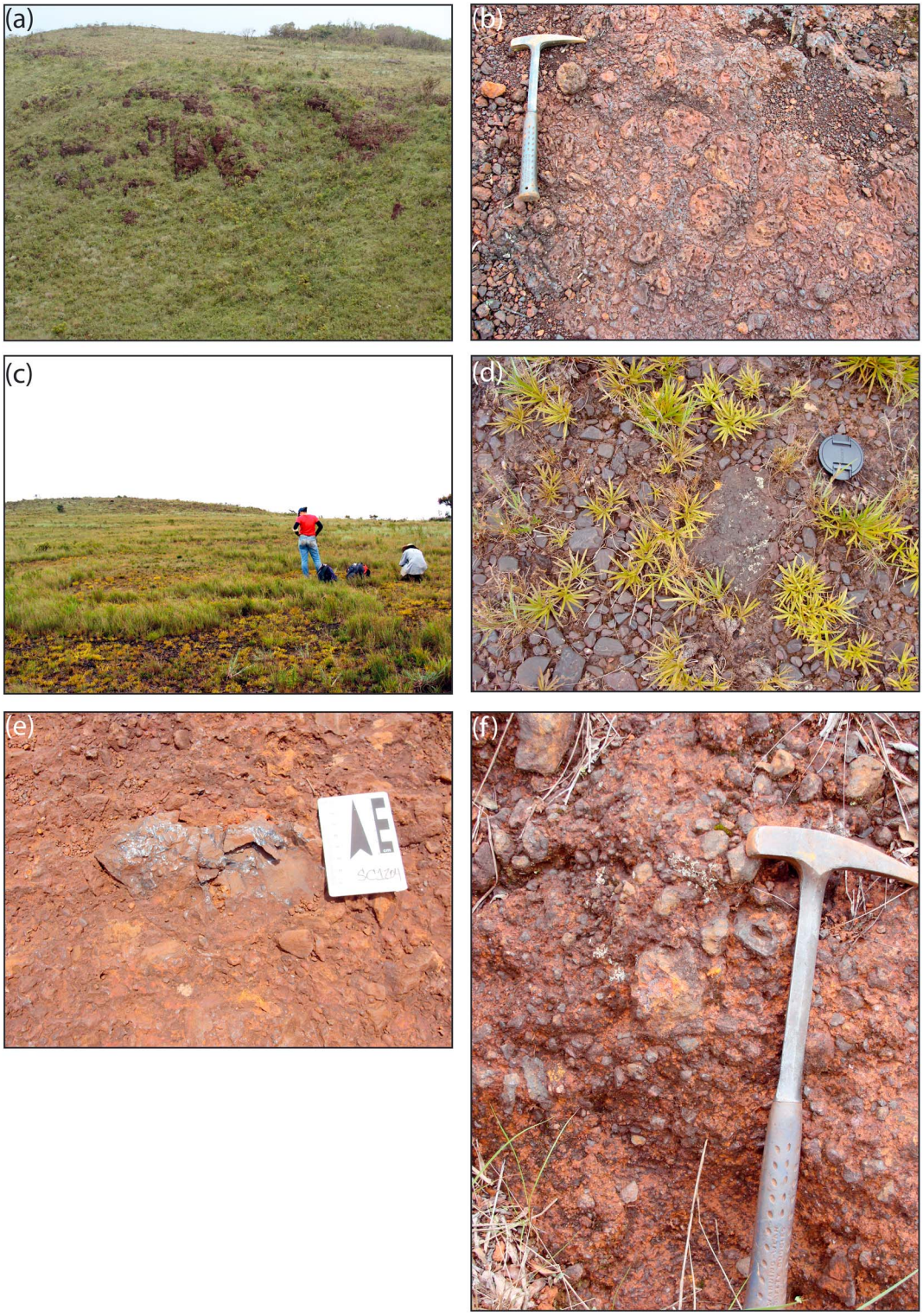

Figure 2. (a) Undulating plateau surfaces are underlain by canga blankets that undergo erosion by rill incision and scarp retreat at plateau edges. (b) The canga blanket shows a complex history of goethite cementation, fragmentation, and recementation. (c) Partial dismantling of the canga blanket generates a (d) colluvial layer composed of loose fragments of hematite-magnetite ore and transported canga blocks that provide useful material for cosmogenic ^{3}He quantification. (e) Fragments of massive goethite veins cemented into canga and (f) fragments of canga in colluvium yield some of the oldest (U-Th)/He results in this study.

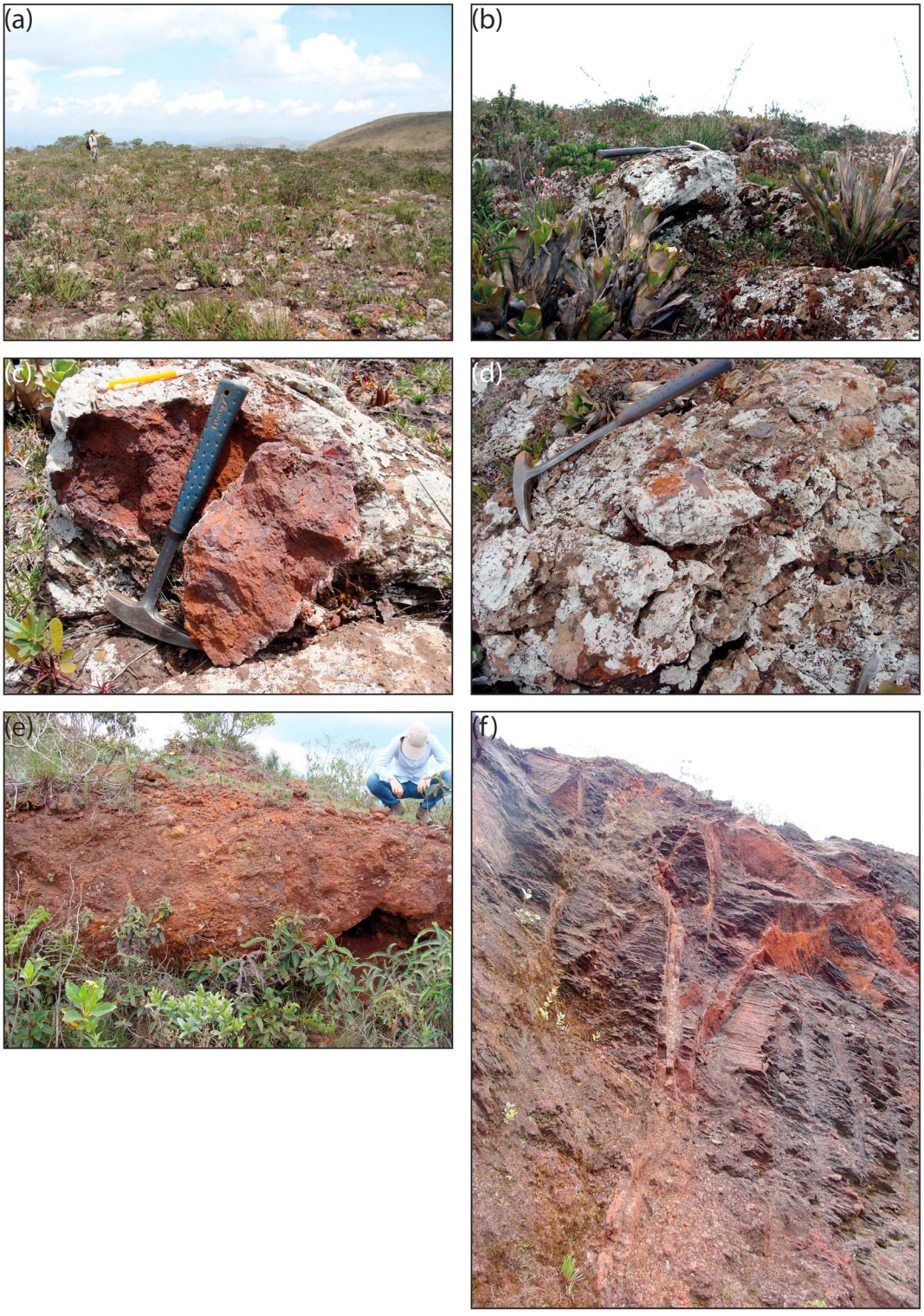

Figure 3. (a) The higher-elevation and more extensive Gandarela plateau is underlain by the thickest and most continuous canga blanket in the region (Baltazar et al., 2005a; Carlos et al., 2014). (b) Boulders of canga covered in lichen and protruding 20–50 cm from the surface reveal the mechanisms (biogeochemical dissolution and physical disaggregation) partially responsible for the very slow destruction of cangas. (c) Fragments of canga or (d) hematite-magnetite ore cemented in cangas were microdrilled for quantifying the vertical concentration of ^{3}He. (e) Cobbles and pebbles of hematite–magnetite ore in transported cangas on top of the Gandarela plateau suggest the existence of a paleo drainage system above the present topographic level. (f) Veins of goethite in saprolite provide some of the oldest goethites dated in this study.

depth, two canga blocks (~ 15 × 15 cm), collected at ~5 km from each other at slightly different elevations on the Gandarela plateau (Figures 1 and 3a–3d), were drilled (2 cm (ID) × 7 cm long drill bit) and the cores sliced every half or 1 cm.

Goethite grains for (U-Th)/He geochronology were selected, prepared, and analyzed following procedures outlined in Monteiro et al. (2014). Samples for ^{3}He measurements were prepared in three ways: (1) crushing canga blocks and picking massive goethite and hematite fragments; (2) microdrilling (5 mm (ID) diamond drill bit) canga-cemented hematite clasts; and (3) microdrilling rounded loose pebbles of hematite collected from plateau surfaces or within small channels draining the plateaus. Canga fragments and drill cores were crushed, sieved, ultrasonically cleaned, washed with acetone or absolute ethanol, and air dried. For the microdrilled samples, magnetic separation was used to isolate magnetic from nonmagnetic fractions. The magnetic fraction, composed mostly of hypogene magnetite-hematite, was preferentially selected for ^{3}He analyses. Representative aliquots of goethites selected for geochronology and cosmogenic ^{3}He measurements were mounted in epoxy disks, polished, and investigated by optical and electron microscopy. A separate aliquot was powdered and studied by X-ray diffractometry (XRD). Mineralogical investigation followed procedures outlined in Monteiro et al. (2014).

(U-Th)/He geochronology followed procedures outlined in Shuster et al. (2005), Vasconcelos et al. (2013), and Monteiro et al. (2014). Isothermal holding time modeling confirms that most goethites retain more than 80% of their radiogenic He budget throughout their lifetime (Heim, et al. 2006; Waltenberg, 2012; Vasconcelos, et al., 2013), suggesting that the error propagation used in this study (adding 10% to the age and imposing a ±10% uncertainty) provides a reasonable estimation of the precipitation ages for the grains analyzed. Dating multiple aliquots may help to identify and eliminate obvious outliers associated with the possible presence of hypogene contaminants (Monteiro et al., 2014), further suggesting that the (U-Th)/He results record ages of mineral precipitation. The coexistence of several goethite generations in a single grain may result in mixed ages, a difficult problem to obviate.

Between ~5 and 50 mg of sample were loaded in Sn foil packets and degassed at 1200°C in a resistance furnace. Reextracts were performed to assure complete gas extraction. Analytical procedures are described elsewhere (Amidon & Farley, 2011; Patterson & Farley, 1998).

To calculate apparent exposure ages for each sample, we used a sea level high-latitude ^{3}He production rate of 68.1 ± 8.1 atoms g^{-1} yr^{-1} for hematite, 71.5 ± 8.5 atoms g^{-1} yr^{-1} for goethite (Shuster et al., 2012), and 64.7 ± 7 atoms g^{-1} yr^{-1} for magnetite (~5% less than P ^{3}He for hematite, as suggested by Masarik, 2002) corrected for latitude and elevation following procedures outlined in Stone (2000). For samples containing more than one mineral, we estimated the relative proportions of each species by petrographic observation of representative aliquots and calculated total ^{3}He production based on the proportions of each mineral phase. As some samples show evidence for continuous exposure (discussed below), we cast the same results in terms of erosion rates by using an average density of 2.88 g/cm^3 (Santos, 2006) for cangas and calculate erosion rates ($\dot{e}$ in g/cm^2/yr) as $\dot{e} = P\Lambda/N$, where P is the production rate (atoms/g/yr), Λ is an attenuation lengthscale (160 g/cm^2), and N is the nuclide concentration (atom/g) measured at the surface (Lal, 1991). For goethite samples where (U-Th)/He ages suggest recrystallization in the more recent past, only the oldest exposure ages (or slowest erosion rates) are relevant. Similarly, magnetite–hematite grains may contain areas partially recrystallized to goethite, which potentially results in partial ^{3}He loss. Therefore, we interpret all results as minimum values and refer to all results as apparent exposure ages (*aEA*).

4. Results

4.1. Mineralogy

Goethite, hematite, martite (hematite pseudomorph after magnetite), and magnetite are the Fe-bearing phases identified by optical microscopy, XRD, and SEM investigation of samples used in this study. Hematite and magnetite are often partially altered to goethite (Figures 4a and 4b). Pure goethite masses commonly show evidence of several generations intimately intergrown (Figures 4c and 4d); goethite masses may also contain small amounts of supergene gibbsite and rarely quartz. Goethite often shows evidence of ferruginized tree roots and bacterial fossils, attesting to the strong role of the biota in iron cementation (Levett et al., 2016; Monteiro et al., 2014).

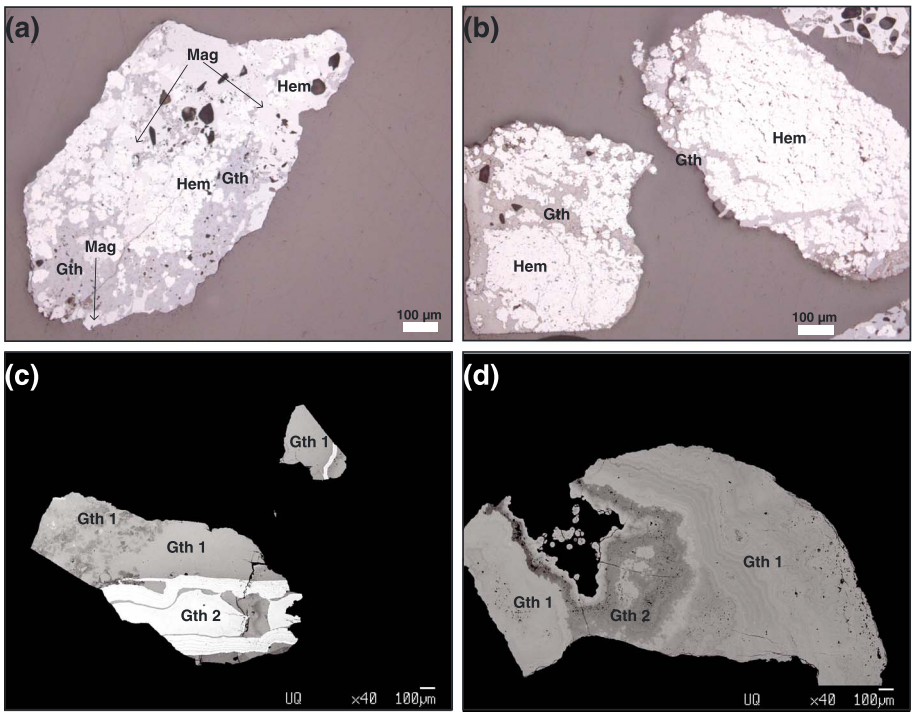

Figure 4. Photomicrographs of representative samples used in ^{3}He measurements reveal (a, b) the complex mineralogy (Hem = hematite, Mag = magnetite, and Gth = goethite) and (c, d) several generations of goethite (Gth 1, Gth 2) showing BSE contrast between first-generation dark cryptocrystalline Al-rich and porous goethite and bright bands of microcrystalline (20–30 µm long) Al-poor densely packed goethite. (c, d) The colloform nature of the goethite cements record the duration of mineral precipitation.

4.2. (U-Th)/He Ages

We report new and previously published (Monteiro et al., 2014) (U-Th)/He goethite precipitation ages (*pAs*) (n = 157). New goethite (U-Th)/He results come from plateau surfaces (n = 86), detrital canga fragments deposited in colluvia (n = 19), and saprolites (n = 30) (Table 1; Figures 5 and 6). Goethites cementing cangas at Serra do Gandarela yield, on average, older results (53.2–0.8 Ma, n = 104) than those obtained for goethites from Serra da Moeda (37.9–0.4 Ma, n = 49) and Serra das Serrinhas (24.3–0.4 Ma, n = 77) (Table 1; Figure 5a). Goethites from saprolites at the three sites are, on average, older than goethite cements from cangas (Table 1; Figures 5a and 6).

4.3. Cosmogenic ^{3}He Concentrations, *Minimum Surface Exposure Ages*, and Erosion Rates

Fifteen goethite samples previously dated by (U-Th)/He and 60 hematite-magnetite-martite samples were analyzed for cosmogenic ^{3}He. Most samples yield significant concentrations of ^{3}He (Table 2), which we interpret to be cosmogenic (Shuster et al., 2012). Hematite-magnetite and martite grains yield higher ^{3}He contents than coexisting goethite cements (e.g., samples 1A, 1B, and 1C; Table 2), but significant ^{3}He concentrations also occur in goethite grains (e.g., sample 21; Table 2). Interestingly, a single canga block may display a significant range of ^{3}He concentrations, as illustrated by the results obtained along 7 cm long, 2 cm wide drill cores from samples G1201 and G1209 (Table 2; Figure 7). Detrital fragments and pebbles show ^{3}He concentrations larger than or equal to those measured from immediately adjacent and partially dismantled canga blocks (Figures 5a and 5c; Table 2).

When cast in terms of apparent exposure ages *(aEA),* the ^{3}He results reveal that the thicker and more laterally continuous canga blankets at Gandarela record a longer exposure history than the thinner and intermittent cangas at Serras da Moeda and das Serrinhas (Figure 5; Table 2). But the longest *aEA*s were obtained for hematite-magnetite clasts eroded from cangas and pebbles collected in colluvia or creeks draining the plateaus (Figures 5a and 5c; Table 2).

Journal of Geophysical Research: Earth Surface

10.1002/2017JF004282

Table 1

Published and New (U-Th)/He Results for Quadrilátero Ferrífero Goethite Cements From Regional Duricrusts, Saprolites and Colluvia

Site	Sample name[a]	Weathering stage	Latitute/ longitude	Elevation (m)	Depth (m)	Measured He Age (ma)	Corrected He Age (ma)[b]	±	He (nmol/g)	±	U (ppm)	±	Th (ppm)	±	Th/U	Mass (μg)
Serra das Serrinhas	Pic-06-01A/1	Duricrust	20° 15′ 23.72″S 43° 52′ 43.88″W	1,495	0	1.7	1.8	0.2	0.0058	0.0021	0.30	0.01	1.45	0.05	4.83	199.70
	Pic-06-01A/1a	Duricrust		1,495	0	4.2	4.7	0.5	0.0306	0.0013	0.47	0.02	3.68	0.08	7.83	50.64
	Pic-06-01A/1b[a]	Duricrust		1,495	0	1.6	1.8	0.2	0.0115	0.0007	0.46	0.02	3.63	0.11	7.88	29.02
	Pic-06-01A/2[a]	Duricrust		1,495	0	0.7	0.8	0.2	0.0039	0.0020	0.49	0.02	2.06	0.05	4.20	52.94
	Pic-06-01A/3	Duricrust		1,495	0	2.7	2.9	0.3	0.0098	0.0022	0.31	0.01	1.58	0.05	5.10	175.25
	Pic-06-01A/4	Duricrust		1,495	0	3.0	3.3	0.3	0.0145	0.0023	0.31	0.01	2.51	0.06	8.10	119.79
	Pic-06-01A/4a[a]	Duricrust		1,495	0	0.6	0.7	0.1	0.0037	0.0008	0.30	0.01	3.32	0.07	11.18	76.26
	Pic-06-01A/4b[a]	Duricrust		1,495	0	0.5	0.6	0.1	0.0022	0.0006	0.20	0.01	2.32	0.05	11.37	81.61
	Pic-06-01A/4c[a]	Duricrust		1,495	0	0.4	0.4	0.1	0.0028	0.0007	0.36	0.01	4.16	0.08	11.66	83.06
	Pic-06-01A/5b[a]	Duricrust		1,495	0	1.6	1.7	0.3	0.0027	0.0007	0.12	0.01	0.80	0.03	6.50	106.22
	Pic-06-01A/5c[a]	Duricrust		1,495	0	0.5	0.6	0.1	0.0017	0.0006	0.14	0.01	1.96	0.04	13.88	128.49
	Pic-06-01A/6a[a]	Duricrust		1,495	0	1.2	1.4	0.2	0.0053	0.0007	0.31	0.02	2.03	0.06	6.45	48.13
	Pic-06-01A/6b[a]	Duricrust		1,495	0	0.7	0.8	0.4	0.0019	0.0004	0.18	0.01	1.33	0.05	7.36	51.32
	Pic-06-01A/6c	Duricrust		1,495	0	2.5	2.7	0.3	0.0163	0.0010	0.41	0.02	3.41	0.08	8.29	56.33
	Pic-06-01A/7a[a]	Duricrust		1,495	0	0.8	0.9	0.5	0.0018	0.0004	0.17	0.01	0.90	0.05	5.26	49.43
	Pic-06-01A/7b[a]	Duricrust		1,495	0	0.6	0.7	0.2	0.0019	0.0005	0.15	0.01	1.72	0.05	11.09	72.24
	Pic-06-01A/7c[a]	Duricrust		1,495	0	0.4	0.4	0.2	0.0013	0.0004	0.20	0.01	2.05	0.05	10.49	68.16
	Pic-06-01A/8a	Duricrust		1,495	0	1.9	2.1	0.2	0.0285	0.0012	0.61	0.02	9.06	0.15	14.97	54.63
	Pic-06-01A/8b[a]	Duricrust		1,495	0	0.4	0.5	0.2	0.0016	0.0005	0.23	0.01	2.06	0.05	9.15	68.43
	Pic-06-01A/8c	Duricrust		1,495	0	3.4	3.7	0.4	0.0178	0.0010	0.31	0.01	2.81	0.07	8.98	52.93
	Pic-06-01B/1	Duricrust	20° 15′ 23.72″S 43° 52′ 43.88″W	1,495	0	1.4	1.5	0.2	0.0051	0.0020	0.30	0.01	1.62	0.05	5.40	119.53
	Pic-06-01B/3	Duricrust		1,495	0	2.7	2.9	0.3	0.0214	0.0025	0.64	0.02	3.55	0.07	5.55	139.68
	Pic-06-01B/3a	Duricrust		1,495	0	2.3	2.6	0.3	0.0136	0.0023	0.38	0.02	2.94	0.07	7.84	54.94
	Pic-06-01B/3b	Duricrust		1,495	0	2.3	2.5	0.3	0.0160	0.0024	0.50	0.02	3.29	0.07	6.63	84.29
	Pic-06-01B/3c	Duricrust		1,495	0	2.2	2.5	0.2	0.0101	0.0022	0.35	0.02	2.08	0.06	5.97	63.26
	Pic-06-01B/4	Duricrust		1,495	0	1.3	1.5	0.1	0.0080	0.0021	0.50	0.02	2.60	0.06	5.20	72.78
	Pic-06-01B/5a	Duricrust		1,495	0	1.9	2.1	0.2	0.0069	0.0021	0.19	0.01	2.00	0.05	10.30	90.85
	Pic-06-01B/5b[a]	Duricrust		1,495	0	1.3	1.4	0.2	0.0054	0.0021	0.22	0.01	2.36	0.06	10.58	69.01
	Pic-06-01B/5c	Duricrust		1,495	0	1.3	1.4	0.1	0.0074	0.0021	0.37	0.01	2.95	0.05	8.06	126.01
	Pic-06-01C/2	Duricrust	20° 15′ 23.72″S 43° 52′ 43.88″W	1,495	0	3.3	3.6	0.4	0.0568	0.0036	1.30	0.03	8.09	0.12	6.22	187.83
	Pic-06-01C/2a	Duricrust		1,495	0	3.1	3.4	0.3	0.1070	0.0050	2.66	0.06	15.89	0.23	5.97	51.04
	Pic-06-01C/2b	Duricrust		1,495	0	2.7	2.9	0.3	0.0297	0.0028	0.78	0.03	5.39	0.10	6.90	68.87
	Pic-06-01C/2c	Duricrust		1,495	0	5.1	5.6	0.6	0.0554	0.0035	0.81	0.02	5.01	0.09	6.22	87.64
	Pic-06-01C/3	Duricrust		1,495	0	2.6	2.8	0.3	0.0345	0.0029	0.96	0.02	6.37	0.10	6.64	75.99
	Pic-06-01C/5	Duricrust		1,495	0	2.5	2.8	0.3	0.0230	0.0026	0.76	0.02	3.87	0.07	5.09	109.29
	Pic-06-01C/6a	Duricrust		1,495	0	5.5	6.1	0.6	0.3310	0.0115	3.61	0.07	31.45	0.36	8.72	58.05
	Pic-06-01C/6b	Duricrust		1,495	0	6.0	6.6	0.7	0.0711	0.0040	0.71	0.02	6.19	0.10	8.73	91.73
	Pic-06-01C/6c	Duricrust		1,495	0	1.8	2.0	0.2	0.0117	0.0022	0.75	0.02	1.91	0.04	2.55	121.47
	Pic-06-02/1	Duricrust	20° 15′ 23.47″S 43° 52′ 43.50″W	1,490	5	0.8	0.9	0.1	0.0038	0.0020	0.47	0.02	1.79	0.05	3.81	119.04
	Pic-06-02/2	Duricrust		1,490	5	0.9	0.9	0.1	0.0055	0.0021	0.57	0.02	2.55	0.06	4.47	96.24
	Pic-06-02/4[a]	Duricrust		1,490	5	1.5	1.7	0.2	0.0066	0.0021	0.37	0.01	1.79	0.05	4.84	62.97
	Pic-06-02/5[a]	Duricrust		1,490	5	1.3	1.4	0.2	0.0108	0.0022	0.83	0.02	3.15	0.06	3.80	31.83
	Pic-06-02/6	Duricrust		1,490	5	1.0	1.1	0.1	0.0066	0.0021	0.75	0.02	2.19	0.05	2.92	81.32
	Pic-06-02/7	Duricrust		1,490	5	1.9	2.1	0.2	0.0159	0.0024	0.76	0.02	3.24	0.07	4.26	103.08
	Pic-06-02/8	Duricrust		1,490	5	1.6	1.8	0.2	0.0128	0.0023	0.79	0.02	2.86	0.06	3.62	74.56
	Pic-06-02/9[a]	Duricrust		1,490	5	0.7	0.7	0.2	0.0037	0.0020	0.49	0.02	2.12	0.05	4.33	45.06
	Pic-06-02/10a[a]	Duricrust		1,490	5	1.9	2.0	0.3	0.0033	0.0020	0.14	0.01	0.81	0.03	5.76	95.55

Journal of Geophysical Research: Earth Surface

10.1002/2017JF004282

Table 1 *(continued)*

Site	Sample name[a]	Weathering stage	Latitute/ longitude	Elevation (m)	Depth (m)	Measured He Age (ma)	Corrected He Age (ma)[b]	±	He (nmol/g)	±	U (ppm)	±	Th (ppm)	±	Th/U	Mass (μg)
	Pic-06-02/10b[a]	*Duricrust*		*1,490*	*5*	*1.6*	*1.8*	*0.3*	*0.0053*	*0.0021*	*0.24*	*0.01*	*1.49*	*0.05*	*6.15*	*57.54*
	Pic-06-02/10c[a]	*Duricrust*		*1,490*	*5*	*1.6*	*1.7*	*0.3*	*0.0044*	*0.0020*	*0.18*	*0.01*	*1.40*	*0.04*	*7.75*	*69.47*
	Pic-06-02/11a[a]	*Duricrust*		*1,490*	*5*	*0.4*	*0.5*	*0.1*	*0.0012*	*0.0019*	*0.16*	*0.01*	*1.58*	*0.03*	*9.68*	*184.89*
	Pic-06-02/11b[a]	*Duricrust*		*1,490*	*5*	*1.7*	*1.9*	*0.2*	*0.0046*	*0.0020*	*0.19*	*0.01*	*1.29*	*0.04*	*6.80*	*78.73*
	Pic-06-02/11c[a]	*Duricrust*		*1,490*	*5*	*1.0*	*1.1*	*0.2*	*0.0027*	*0.0020*	*0.15*	*0.01*	*1.54*	*0.04*	*10.48*	*106.33*
	Pic-06-03/1	*Duricrust*	20° 15′ 23.79″S	*1,480*	*15*	*14.3*	*15.7*	*1.6*	*0.4367*	*0.0146*	*2.44*	*0.05*	*13.53*	*0.17*	*5.55*	*103.64*
	Pic-06-03/2	*Duricrust*	43° 52′ 43.88″W	*1,480*	*15*	*9.9*	*10.8*	*1.1*	*0.3537*	*0.0122*	*5.64*	*0.10*	*4.09*	*0.07*	*0.73*	*67.91*
	Pic-06-03/3	*Duricrust*		*1,480*	*15*	*3.0*	*3.3*	*0.3*	*0.0713*	*0.0040*	*2.06*	*0.04*	*9.68*	*0.13*	*4.70*	*102.81*
	Pic-06-03/4	*Duricrust*		*1,480*	*15*	*12.7*	*14.0*	*1.4*	*0.3097*	*0.0109*	*2.30*	*0.05*	*9.25*	*0.13*	*4.02*	*125.88*
	Pic-06-03/5	*Duricrust*		*1,480*	*15*	*18.3*	*20.1*	*2.0*	*0.4459*	*0.0149*	*3.62*	*0.07*	*3.68*	*0.07*	*1.02*	*146.97*
	Pic-06-03/6a	*Duricrust*		*1480*	*15*	*22.1*	*24.4*	*2.4*	*0.3463*	*0.0120*	*2.22*	*0.04*	*2.79*	*0.05*	*1.26*	*112.38*
	Pic-06-03/6b	*Duricrust*		*1,480*	*15*	*17.6*	*19.3*	*1.9*	*0.5129*	*0.0168*	*2.83*	*0.05*	*10.77*	*0.15*	*3.80*	*78.05*
	Pic-06-03/6c	*Duricrust*		*1,480*	*15*	*6.7*	*7.4*	*0.7*	*0.3630*	*0.0125*	*2.57*	*0.04*	*31.30*	*0.28*	*12.18*	*122.47*
	Pic-06-07/1[a]	*Duricrust*	20° 12′ 38.52″S	*1,554*	*1*	*0.4*	*0.4*	*0.1*	*0.0040*	*0.0020*	*1.35*	*0.03*	*2.07*	*0.05*	*1.53*	*95.20*
	Pic-06-07/1a[a]	*Duricrust*	43° 51′ 10.76″W	*1,554*	*1*	*0.7*	*0.8*	*0.1*	*0.0065*	*0.0004*	*1.22*	*0.04*	*2.00*	*0.06*	*1.64*	*47.90*
	Pic-06-07/1b	*Duricrust*		*1,554*	*1*	*1.7*	*1.9*	*0.2*	*0.0323*	*0.0007*	*2.60*	*0.07*	*3.83*	*0.10*	*1.47*	*37.23*
	Pic-06-07/1c	*Duricrust*		*1,554*	*1*	*0.7*	*0.8*	*0.1*	*0.0157*	*0.0005*	*2.95*	*0.07*	*4.47*	*0.10*	*1.51*	*39.64*
	Pic-06-07/5a	*Duricrust*		*1,554*	*1*	*1.2*	*1.3*	*0.1*	*0.0147*	*0.0005*	*1.67*	*0.05*	*2.47*	*0.07*	*1.48*	*42.38*
	Pic-06-07/5b	*Duricrust*		*1,554*	*1*	*0.8*	*0.9*	*0.1*	*0.0177*	*0.0008*	*3.48*	*0.06*	*2.80*	*0.06*	*0.80*	*81.79*
	Pic-06-07/5c	*Duricrust*		*1,554*	*1*	*2.8*	*3.1*	*0.3*	*0.2400*	*0.0036*	*9.66*	*0.15*	*24.85*	*0.35*	*2.57*	*33.18*
	Pic-06-08/2[a]	*Duricrust*	20° 12′ 38.09″S	*1,555*	*0*	*1.2*	*1.3*	*0.1*	*0.0045*	*0.0020*	*0.54*	*0.02*	*0.62*	*0.04*	*1.15*	*89.85*
	Pic-06-08/6b	*Duricrust*	43° 51′ 11.17″W	*1,555*	*0*	*3.9*	*4.2*	*0.4*	*0.1007*	*0.0018*	*3.37*	*0.08*	*6.08*	*0.13*	*1.80*	*39.36*
	Pic-06-08/6c	*Duricrust*		*1,555*	*0*	*3.2*	*3.5*	*0.4*	*0.0879*	*0.0014*	*3.60*	*0.09*	*6.01*	*0.14*	*1.67*	*32.06*
	Pic-06-08/7a	*Duricrust*		*1,555*	*0*	*1.9*	*2.0*	*0.2*	*0.0189*	*0.0009*	*1.29*	*0.03*	*2.48*	*0.05*	*1.93*	*92.08*
	Pic-06-08/7b	*Duricrust*		*1,555*	*0*	*1.7*	*1.8*	*0.2*	*0.0117*	*0.0008*	*0.91*	*0.02*	*1.61*	*0.04*	*1.77*	*116.39*
	Pic-06-08/7c	*Duricrust*		*1,555*	*0*	*2.4*	*2.7*	*0.3*	*0.0146*	*0.0010*	*0.82*	*0.02*	*1.25*	*0.03*	*1.53*	*125.01*
	Pic-06-08/9a	*Duricrust*		*1,555*	*0*	*2.4*	*2.6*	*0.3*	*0.0114*	*0.0006*	*0.59*	*0.02*	*1.19*	*0.04*	*2.01*	*60.49*
	Pic-06-08/9b	*Duricrust*		*1,555*	*0*	*5.0*	*5.5*	*0.6*	*0.1174*	*0.0033*	*3.05*	*0.06*	*5.31*	*0.10*	*1.74*	*61.54*
	Pic-06-08/9c	*Duricrust*		*1,555*	*0*	*3.8*	*4.2*	*0.4*	*0.0506*	*0.0019*	*1.72*	*0.04*	*3.12*	*0.06*	*1.81*	*81.61*
	Pic-06-13/4	*Duricrust*	20° 08′ 59.89″S 43° 52′ 34.19″W	*1,378*	*0*	*0.6*	*0.7*	*0.1*	*0.0091*	*0.0022*	*2.23*	*0.05*	*2.32*	*0.06*	*1.04*	*120.72*
	Pic-06-04/2	*Saprolite*	20° 15′ 23.79″S	*1,475*	*20*	*26.7*	*29.4*	*2.9*	*0.6041*	*0.0195*	*4.06*	*0.08*	*0.36*	*0.03*	*0.09*	*99.95*
	Pic-06-04/2a	*Saprolite*	43° 52′ 43.88″W	*1,475*	*20*	*26.0*	*28.6*	*2.9*	*0.4249*	*0.0143*	*2.98*	*0.06*	*0.06*	*0.03*	*0.02*	*59.58*
	Pic-06-04/2b	*Saprolite*		*1,475*	*20*	*50.3*	*55.3*	*5.5*	*0.8532*	*0.0267*	*3.09*	*0.07*	*0.06*	*0.04*	*0.02*	*47.68*
	Pic-06-04/2c	*Saprolite*		*1,475*	*20*	*29.0*	*31.9*	*3.2*	*0.4899*	*0.0162*	*3.09*	*0.05*	*0.04*	*0.02*	*0.01*	*100.57*
	Pic-06-04/3	*Saprolite*		*1,475*	*20*	*27.4*	*30.1*	*3.0*	*0.3496*	*0.0121*	*2.29*	*0.05*	*0.22*	*0.03*	*0.10*	*161.38*
	Pic-06-04/3a	*Saprolite*		*1,475*	*20*	*31.3*	*34.5*	*3.4*	*0.3779*	*0.0129*	*2.20*	*0.05*	*0.05*	*0.02*	*0.02*	*78.64*
	Pic-06-04/3b	*Saprolite*		*1,475*	*20*	*31.6*	*34.8*	*3.5*	*0.3763*	*0.0128*	*2.17*	*0.04*	*0.05*	*0.02*	*0.02*	*97.62*
	Pic-06-04/3c	*Saprolite*		*1,475*	*20*	*26.7*	*29.3*	*2.9*	*0.3681*	*0.0126*	*2.52*	*0.05*	*0.06*	*0.02*	*0.02*	*79.05*
	Pic-06-05B/2	*Saprolite*	20° 15′ 17.78″S 43° 52′ 41.27″W	*1,465*	*30*	*23.3*	*25.7*	*2.6*	*0.5913*	*0.0191*	*4.56*	*0.08*	*0.46*	*0.04*	*0.10*	*183.70*
Serra Do Gandarela	*Pic-06-21/5*	*Duricrust*	20° 07′ 5.48″S	*1,651*	*0*	*8.3*	*9.1*	*0.9*	*0.0740*	*0.0041*	*0.80*	*0.02*	*3.59*	*0.07*	*4.49*	*137.77*
	Pic-06-21/6 a	*Duricrust*	43° 39′ 38.02″W	*1,651*	*0*	*27.0*	*29.7*	*3.0*	*0.6569*	*0.0260*	*2.62*	*0.05*	*7.87*	*0.12*	*3.01*	*88.32*
	Pic-06-21/6 b	*Duricrust*		*1,651*	*0*	*16.0*	*17.6*	*1.8*	*0.5454*	*0.0180*	*2.55*	*0.05*	*15.79*	*0.20*	*6.20*	*73.72*
	Pic-06-21/6 c	*Duricrust*		*1,651*	*0*	*17.7*	*19.4*	*1.9*	*0.7843*	*0.0324*	*3.20*	*0.05*	*21.08*	*0.23*	*6.59*	*92.08*
	Pic-06-21/6 d	*Duricrust*		*1,651*	*0*	*10.7*	*11.8*	*1.2*	*0.3641*	*0.0202*	*3.54*	*0.04*	*11.44*	*0.14*	*3.23*	*123.72*
	Pic-06-21/6 e	*Duricrust*		*1,651*	*0*	*20.0*	*21.9*	*2.2*	*0.4772*	*0.0160*	*1.74*	*0.04*	*11.30*	*0.16*	*6.51*	*74.54*
	Pic-06-21/6 f	*Duricrust*		*1,651*	*0*	*26.5*	*29.2*	*2.9*	*0.7024*	*0.0201*	*2.51*	*0.05*	*10.01*	*0.15*	*3.99*	*63.76*

Table 1 *(continued)*

Site	Sample name[a]	Weathering stage	Latitute/ longitude	Elevation (m)	Depth (m)	Measured He Age (ma)	Corrected He Age (ma)[b]	±	He (nmol/g)	±	U (ppm)	±	Th (ppm)	±	Th/U	Mass (μg)
	Pic-06-21/6 g	*Duricrust*		*1,651*	*0*	*23.6*	*25.9*	*2.6*	*0.4419*	*0.0218*	*1.83*	*0.04*	*6.87*	*0.10*	*3.76*	*110.01*
	Pic-06-21/6 h	*Duricrust*		*1,651*	*0*	*21.4*	*23.5*	*2.3*	*0.3645*	*0.0134*	*1.57*	*0.04*	*6.66*	*0.11*	*4.25*	*81.98*
	Pic-06-21/6 i	*Duricrust*		*1,651*	*0*	*18.0*	*19.8*	*2.0*	*0.4401*	*0.0147*	*1.61*	*0.04*	*12.24*	*0.17*	*7.60*	*73.41*
	Pic-06-21/6 j	*Duricrust*		*1,651*	*0*	*12.7*	*13.9*	*1.4*	*0.6244*	*0.0156*	*3.26*	*0.07*	*24.67*	*0.30*	*7.57*	*55.57*
	Pic-06-21/6 l	*Duricrust*		*1,651*	*0*	*18.1*	*20.0*	*2.0*	*0.1975*	*0.0126*	*0.90*	*0.02*	*4.69*	*0.07*	*5.23*	*142.10*
	Pic-06-21/6 m	*Duricrust*		*1,651*	*0*	*15.6*	*17.1*	*1.7*	*0.5978*	*0.0212*	*2.94*	*0.05*	*17.49*	*0.21*	*5.96*	*79.19*
	Pic-06-21/6 n	*Duricrust*		*1,651*	*0*	*20.4*	*22.5*	*2.2*	*0.4532*	*0.0215*	*1.77*	*0.04*	*9.83*	*0.13*	*5.57*	*105.87*
	Pic-06-21/6 o	*Duricrust*		*1,651*	*0*	*14.5*	*15.9*	*1.6*	*0.5587*	*0.0203*	*2.57*	*0.05*	*19.20*	*0.23*	*7.47*	*81.03*
	Pic-06-21/6 p	*Duricrust*		*1,651*	*0*	*13.6*	*15.0*	*1.5*	*0.4487*	*0.0217*	*2.83*	*0.04*	*13.67*	*0.16*	*4.83*	*107.86*
	Pic-06-21/6 q	*Duricrust*		*1,651*	*0*	*17.5*	*19.2*	*1.9*	*0.5468*	*0.0188*	*2.17*	*0.05*	*15.22*	*0.19*	*7.03*	*76.47*
	Pic-06-21/6 r	*Duricrust*		*1,651*	*0*	*21.9*	*24.1*	*2.4*	*0.8249*	*0.0284*	*2.98*	*0.05*	*16.72*	*0.21*	*5.61*	*76.79*
	Pic-06-21/6 s	*Duricrust*		*1,651*	*0*	*15.1*	*16.6*	*1.7*	*0.3735*	*0.0180*	*2.62*	*0.04*	*8.19*	*0.11*	*3.12*	*107.70*
	Pic-06-21/6 t	*Duricrust*		*1,651*	*0*	*20.9*	*23.0*	*2.3*	*0.4029*	*0.0148*	*1.68*	*0.04*	*7.95*	*0.12*	*4.74*	*82.01*
	Pic-06-21/6 u	*Duricrust*		*1,651*	*0*	*18.4*	*20.2*	*2.0*	*0.4516*	*0.0194*	*2.23*	*0.04*	*9.74*	*0.13*	*4.37*	*95.99*
	Pic-06-21-1G-1a	*Duricrust*		*1,651*	*0*	*26.3*	*28.9*	*2.9*	*0.4039*	*0.0247*	*1.20*	*0.02*	*6.90*	*0.09*	*5.77*	*136.28*
	Pic-06-21-1G-1b	*Duricrust*		*1,651*	*0*	*26.6*	*29.3*	*2.9*	*0.5166*	*0.0313*	*1.29*	*0.03*	*9.66*	*0.12*	*7.47*	*135.10*
	Pic-06-21-1G-1c	*Duricrust*		*1,651*	*0*	*43.7*	*48.1*	*4.8*	*0.4620*	*0.0128*	*0.30*	*0.01*	*6.96*	*0.12*	*23.16*	*61.62*
	Pic-06-21-1G-2a	*Duricrust*		*1,651*	*0*	*30.2*	*33.2*	*3.3*	*0.2254*	*0.0107*	*0.76*	*0.02*	*2.59*	*0.05*	*3.41*	*105.64*
	Pic-06-21-1G-2b	*Duricrust*		*1,651*	*0*	*28.9*	*31.8*	*3.2*	*0.2939*	*0.0214*	*0.97*	*0.02*	*3.81*	*0.06*	*3.93*	*162.42*
	Pic-06-21-1G-3a	*Duricrust*		*1,651*	*0*	*41.6*	*45.8*	*4.6*	*0.2269*	*0.0076*	*0.45*	*0.02*	*2.33*	*0.05*	*5.14*	*74.50*
	Pic-06-21-1G-3b	*Duricrust*		*1,651*	*0*	*25.9*	*28.5*	*2.8*	*0.2176*	*0.0134*	*0.84*	*0.02*	*3.01*	*0.05*	*3.60*	*136.95*
	Pic-06-21-1G-3c	*Duricrust*		*1,651*	*0*	*23.4*	*25.8*	*2.6*	*0.5254*	*0.0087*	*2.51*	*0.07*	*6.85*	*0.14*	*2.73*	*36.26*
	Pic-06-21-1G-4a	*Duricrust*		*1,651*	*0*	*19.0*	*20.9*	*2.1*	*0.4119*	*0.0075*	*2.22*	*0.06*	*7.54*	*0.14*	*3.40*	*39.17*
	Pic-06-21-1G-4b	*Duricrust*		*1,651*	*0*	*21.3*	*23.5*	*2.3*	*0.5630*	*0.0133*	*2.68*	*0.06*	*9.24*	*0.15*	*3.45*	*52.14*
	Pic21_FG	Duricrust		1,651	0	20.6	22.6	2.3	0.5498	0.0136	2.54	0.06	10.08	0.16	3.97	54.98
	Pic21_FG	Duricrust		1,651	0	25.9	28.5	2.8	0.4575	0.0147	1.52	0.04	7.32	0.12	4.82	71.83
	Pic21_FG	Duricrust		1,651	0	30.6	33.6	3.4	1.3034	0.0232	3.95	0.08	16.46	0.25	4.16	39.81
	Pic-06-21_frostedGt	Duricrust		1,651	0	32.1	35.3	3.5	0.2858	0.0029	1.02	0.03	2.62	0.06	2.58	96.65
	Pic-06-21_frostedGt	Duricrust		1,651	0	30.5	33.5	3.4	0.3315	0.0221	1.11	0.04	3.79	0.10	3.42	43.98
	Pic21_VG	Duricrust		1,651	0	9.7	10.6	1.1	0.7544	0.0127	5.36	0.10	38.32	0.46	7.15	37.37
	Pic21_VG	Duricrust		1,651	0	9.6	10.5	1.1	0.6240	0.0100	5.26	0.10	28.73	0.38	5.47	35.30
	Pic21_VG	Duricrust		1,651	0	11.3	12.5	1.2	0.6682	0.0133	3.40	0.07	31.66	0.38	9.30	44.38
	Pic21_VG	Duricrust		1,651	0	9.5	10.5	1.0	0.6035	0.0269	6.49	0.06	22.05	0.23	3.40	99.33
	Pic21_VG	Duricrust		1,651	0	10.0	11.0	1.1	0.9361	0.0187	8.10	0.11	39.00	0.44	4.82	44.52
	Pic21_VG	Duricrust		1,651	0	11.7	12.8	1.3	0.8223	0.0141	5.34	0.10	32.45	0.41	6.08	38.11
	Pic21_FwVG	Duricrust		1,651	0	17.2	18.9	1.9	1.3388	0.0410	7.61	0.08	28.62	0.31	3.76	68.28
	Pic21_FwVG	Duricrust		1,651	0	16.2	17.9	1.8	0.8160	0.0142	4.68	0.09	19.35	0.28	4.13	38.56
	Pic21_FwVG	Duricrust		1,651	0	14.3	15.7	1.6	0.6645	0.0129	4.61	0.09	16.84	0.25	3.66	43.15
	Pic21_FwVG	Duricrust		1,651	0	19.2	21.1	2.1	1.2544	0.0298	6.00	0.09	25.51	0.31	4.25	52.94
	Pic21_FwVG	Duricrust		1,651	0	17.7	19.4	1.9	0.7766	0.0130	3.73	0.08	18.47	0.27	4.95	37.13
	Pic21_FwVG	Duricrust		1,651	0	17.7	19.5	2.0	0.9613	0.0266	4.79	0.08	21.98	0.27	4.58	61.71
	Pic-06-21-2G-1	*Duricrust*		*1,651*	*0*	*21.0*	*23.1*	*2.3*	*0.0208*	*0.0014*	*0.11*	*0.01*	*0.30*	*0.03*	*2.64*	*55.16*
	Pic-06-21-2G-2	*Duricrust*		*1,651*	*0*	*22.9*	*25.2*	*2.5*	*0.0243*	*0.0025*	*0.13*	*0.01*	*0.27*	*0.01*	*2.01*	*162.84*
	Pic-06-21-2G-3	*Duricrust*		*1,651*	*0*	*28.6*	*31.5*	*3.1*	*0.0299*	*0.0022*	*0.11*	*0.01*	*0.35*	*0.02*	*3.17*	*103.00*
	Pic-06-21-2G-4	*Duricrust*		*1,651*	*0*	*10.8*	*11.9*	*1.2*	*0.0228*	*0.0019*	*0.21*	*0.01*	*0.75*	*0.04*	*3.61*	*61.89*
	Pic-06-21-2G-5	*Duricrust*		*1,651*	*0*	*27.6*	*27.6*	*5.8*	*0.0150*	*0.0018*	*0.09*	*0.01*	*0.05*	*0.02*	*0.61*	*72.40*
	Pic-06-21-2G-6	*Duricrust*		*1,651*	*0*	*16.8*	*18.5*	*1.8*	*0.0557*	*0.0034*	*0.39*	*0.01*	*0.92*	*0.03*	*2.34*	*114.41*
	Pic-06-21-2G-7	*Duricrust*		*1,651*	*0*	*19.8*	*21.7*	*2.2*	*0.0350*	*0.0025*	*0.19*	*0.01*	*0.57*	*0.02*	*2.99*	*105.37*

AGU Journal of Geophysical Research: Earth Surface

10.1002/2017JF004282

Journal of Geophysical Research: Earth Surface

10.1002/2017JF004282

Table 1 *(continued)*

Site	Sample name[a]	Weathering stage	Latitute/ longitude	Elevation (m)	Depth (m)	Measured He Age (ma)	Corrected He Age (ma)[b]	±	He (nmol/g)	±	U (ppm)	±	Th (ppm)	±	Th/U	Mass (μg)
	Pic-06-21-2G-8	*Duricrust*		*1,651*	*0*	*16.5*	*18.1*	*1.8*	*0.0386*	*0.0027*	*0.21*	*0.01*	*0.95*	*0.03*	*4.55*	*120.71*
	Pic-06-21-2G-9	*Duricrust*		*1,651*	*0*	*43.3*	*47.7*	*4.8*	*0.0265*	*0.0024*	*0.10*	*0.005*	*0.07*	*0.01*	*0.72*	*140.29*
	Pic-06-21-2G-10	*Duricrust*		*1,651*	*0*	*22.0*	*22.0*	*5.8*	*0.0141*	*0.0016*	*0.10*	*0.01*	*0.05*	*0.04*	*0.52*	*46.08*
	Pic21_AlPoor Goe	Duricrust		1,651	0	27.4	30.1	3.0	0.0383	0.0019	0.23	0.01	0.11	0.02	0.49	78.54
	Pic21_AlPoor Goe	Duricrust		1,651	0	21.3	23.5	2.3	0.0401	0.0017	0.32	0.01	0.11	0.03	0.36	59.12
	Pic21_AlPoor Goe	Duricrust		1,651	0	24.3	26.7	2.7	0.1628	0.0067	0.63	0.02	2.57	0.05	4.11	90.53
	Pic21_AlPoor Goe	Duricrust		1,651	0	21.8	23.9	2.4	0.0660	0.0037	0.29	0.01	1.12	0.03	3.83	117.58
	Pic21_AlPoor Goe	Duricrust		1,651	0	27.5	30.3	3.0	0.0319	0.0020	0.21	0.01	0.02	0.02	0.12	101.66
	Pic21_AlPoor Goe	Duricrust		1,651	0	27.1	29.8	3.0	0.0271	0.0010	0.17	0.01	0.07	0.02	0.43	78.60
	Pic21_AlPoor Goe	Duricrust		1,651	0	28.8	31.7	3.2	0.1112	0.0054	0.26	0.01	1.90	0.04	7.27	108.25
	Pic21_AlPoor Goe	Duricrust		1,651	0	26.9	29.6	3.0	0.1112	0.0027	0.38	0.02	1.60	0.05	4.20	53.29
	Pic21_AlPoor Goe	Duricrust		1,651	0	32.3	35.5	3.5	0.0658	0.0030	0.26	0.01	0.47	0.02	1.78	89.83
	Pic21_AlPoor Goe	Duricrust		1,651	0	26.8	29.4	2.9	0.1008	0.0054	0.38	0.01	1.32	0.03	3.44	115.55
	Pic21_AlPoor Goe	Duricrust		1,651	0	26.8	29.5	2.9	0.0396	0.0020	0.24	0.01	0.14	0.02	0.59	84.44
	Pic21_AlPoor Goe	Duricrust		1,651	0	27.4	30.1	3.0	0.0570	0.0020	0.24	0.01	0.62	0.04	2.61	60.78
	Pic21_AlPoor Goe	Duricrust		1,651	0	31.6	34.7	3.5	0.0232	0.0017	0.11	0.01	0.09	0.02	0.84	104.16
	Pic21_AlPoor Goe	Duricrust		1,651	0	29.7	32.7	3.3	0.0333	0.0031	0.15	0.01	0.22	0.01	1.47	189.21
	Pic21_AlPoor Goe	Duricrust		1,651	0	48.3	53.2	5.3	0.0301	0.0023	0.09	0.00	0.10	0.01	1.12	172.82
	Pic-06-24/1	*Duricrust*	20° 06′ 45.50″S	*1,506*	*5*	*14.7*	*16.1*	*1.6*	*0.4344*	*0.0145*	*4.56*	*0.08*	*3.39*	*0.07*	*0.74*	*90.85*
	Pic-06-24/2	*Duricrust*	43° 39′ 2.73″W	*1,506*	*5*	*6.7*	*7.4*	*0.7*	*0.1682*	*0.0068*	*4.43*	*0.08*	*0.84*	*0.04*	*0.19*	*70.73*
	Pic-06-24/3[a]	*Duricrust*		*1,506*	*5*	*5.8*	*6.3*	*6.4*	*0.2750*	*0.0099*	*7.55*	*0.13*	*5.23*	*0.09*	*0.69*	*0.16*
	Pic-06-24/4	*Duricrust*		*1,506*	*5*	*10.4*	*11.5*	*1.1*	*0.2665*	*0.0097*	*4.53*	*0.08*	*0.77*	*0.04*	*0.17*	*105.41*
	Pic-06-24/5	*Duricrust*		*1,506*	*5*	*20.7*	*22.8*	*2.3*	*0.2663*	*0.0096*	*2.24*	*0.05*	*0.52*	*0.04*	*0.23*	*197.60*
	G-12-01	Duricrust	20° 05′ 25.39″S	1,643	0	7.15	7.9	0.8	0.179	0.0120	1.27	0.03	14.15	0.16	11.12	148.94
	G-12-01	Duricrust	43° 41′ 2.45″W	1,643	0	29.12	32.0	3.2	0.347	0.0151	0.86	0.03	5.67	0.09	6.62	96.93
	G-12-04A_black	Duricrust	20° 06′ 0.53″S	1,670	0	8.12	8.9	0.9	0.120	0.0038	1.95	0.04	3.30	0.07	1.69	66.98
	G-12-04A_black	Duricrust	43° 40′ 39.2″W	1,670	0	7.21	7.9	0.8	0.074	0.0039	1.39	0.03	2.16	0.05	1.55	112.31
	G-12-04A_black	Duricrust		1,670	0	10.68	11.7	1.2	0.099	0.0060	1.37	0.03	1.45	0.04	1.06	132.06
	G-12-04A_brown	Duricrust		1,670	0	18.79	20.7	2.1	0.192	0.0090	1.02	0.03	3.62	0.07	3.53	103.76
	G-12-04A_brown	Duricrust		1,670	0	21.72	23.9	2.4	0.233	0.0154	1.14	0.03	3.55	0.06	3.12	146.88
	G-12-04A_brown	Duricrust		1,670	0	17.86	19.6	2.0	0.285	0.0091	1.69	0.04	5.31	0.09	3.15	70.78
	G-12-05 Vitreous Black	Duricrust	20° 06′ 0.21″S	1,659	0	0.76	0.8	0.1	0.028	0.0024	1.01	0.02	24.77	0.22	24.52	166.44
	G-12-05 Vitreous Black	Duricrust	43° 40′ 39.37″W	1,659	0	1.54	1.7	0.2	0.039	0.0036	0.36	0.01	18.34	0.17	50.44	195.87
	G-12-05	Duricrust		1,659	0	3.45	3.8	0.4	0.185	0.0040	1.72	0.05	34.56	0.40	20.06	45.41
	G-12-05	Duricrust		1,659	0	5.06	5.6	0.6	0.265	0.0070	1.39	0.04	34.94	0.37	25.21	58.30
	G-12-06	Duricrust	20° 06′ 0.21″S	1,659	0	31.43	34.6	3.5	0.040	0.0042	0.20	0.01	0.12	0.01	0.60	228.55
	G-12-06	Duricrust	43° 40′ 39.37″W	1,659	0	47.98	52.8	5.3	0.074	0.0080	0.24	0.01	0.17	0.01	0.69	240.08
	G-12-06 (Drill-Core)	Duricrust		1,659	0	16.84	18.5	1.9	0.350	0.0199	2.73	0.04	4.66	0.08	1.71	126.73
	G-12-06 (Drill-Core)	Duricrust		1,659	0	23.72	26.1	2.6	0.187	0.0174	1.15	0.02	1.29	0.03	1.13	206.41
	G-12-06 (Drill-Core)	Duricrust		1,659	0	44.30	48.7	4.9	0.376	0.0461	0.92	0.02	2.70	0.04	2.92	273.24
	G-12-06 (Reddish)	Duricrust		1,659	0	8.15	9.0	0.9	0.232	0.0188	3.32	0.04	8.10	0.10	2.44	180.57
	G-12-06 Vitreous Black	Duricrust		1,659	0	7.13	7.8	0.8	0.246	0.0166	4.11	0.04	9.49	0.11	2.31	181.68
	G-12-06 Vitreous Black	Duricrust		1,659	0	7.18	7.9	0.8	0.217	0.0200	3.95	0.04	6.81	0.09	1.72	170.52
	G-12-08	Duricrust	20° 06′ 59.02″S	1,644		13.91	15.3	1.5	0.416	0.0239	4.679	0.053	3.455	0.061	0.74	127.87
	G-12-08	Duricrust	43° 39′ 40.32″W	1,644		14.78	16.3	1.6	0.520	0.0292	4.086	0.051	10.084	0.131	2.47	125.44
	G-12-09	Duricrust	20° 07′ 3.88″S	1,658	0	6.69	7.4	0.7	0.185	0.0137	4.221	0.042	3.723	0.060	0.88	164.78
	G-12-09	Duricrust	43° 39′ 38.97″W	1,658	0	7.03	7.7	0.8	0.185	0.0130	4.297	0.044	2.325	0.044	0.54	156.00
	GA-13-04 Type1	Duricrust		1,134	0	5.18	5.7	0.6	0.051		1.296	0.035	2.208	0.055	1.70	87.86

Journal of Geophysical Research: Earth Surface

10.1002/2017JF004282

Table 1 *(continued)*

Site	Sample name[a]	Weathering stage	Latitute/ longitude	Elevation (m)	Depth (m)	Measured He Age (ma)	Corrected He Age (ma)[b]	±	He (nmol/g)	±	U (ppm)	±	Th (ppm)	±	Th/U	Mass (μg)
	GA-13-04 Type1	Duricrust	20° 01′ 00.1″S 43° 34′ 43.1″W	1,134	0	9.85	10.8	1.1	0.045		0.692	0.026	0.664	0.041	0.96	66.29
	Pic-06-22/5	*Saprolite*	20° 06′ 42.94″S	*1,490*	*10*	*48.6*	*53.5*	*5.4*	*0.1162*	*0.0053*	*0.41*	*0.02*	*0.10*	*0.03*	*0.24*	*107.54*
	Pic-06-22/5a	*Saprolite*	43° 39′ 2.69″W	*1,490*	*10*	*29.0*	*31.9*	*3.2*	*0.0683*	*0.0033*	*0.42*	*0.01*	*0.04*	*0.02*	*0.10*	*105.64*
	Pic-06-22/5b	*Saprolite*		*1,490*	*10*	*27.1*	*29.8*	*3.0*	*0.0627*	*0.0027*	*0.42*	*0.02*	*0.04*	*0.02*	*0.09*	*93.19*
	Pic-06-22/5c	*Saprolite*		*1,490*	*10*	*37.6*	*41.4*	*4.1*	*0.0830*	*0.0055*	*0.40*	*0.01*	*0.04*	*0.01*	*0.09*	*148.13*
	Pic 06 22 gr1_black	Saprolite		1,490	10	18.49	20.3	2.0	0.5096	0.0180	5.02	0.07	0.16	0.02	0.03	78.62
	Pic 06 22 gr2_black	Saprolite		1,490	10	22.24	24.5	2.4	0.4781	0.0220	3.86	0.05	0.37	0.02	0.10	102.48
	Pic 06 22 gr3_black	Saprolite		1,490	10	14.54	16.0	1.6	0.4653	0.0270	5.84	0.04	0.16	0.01	0.03	129.57
	Pic 06 22 gr4_black	Saprolite		1,490	10	15.83	17.4	1.7	0.5036	0.0227	5.80	0.06	0.18	0.02	0.03	100.28
	Pic 06 23 gr1	Saprolite	20° 06′ 42.80″S	1,517		10.10	11.1	1.1	0.1493	0.0040	2.68	0.06	0.17	0.03	0.06	55.80
	Pic 06 23 gr2	Saprolite	43° 39′ 2.64″W	1,517		8.61	9.5	0.9	0.1011	0.0062	2.13	0.03	0.12	0.01	0.06	133.00
	Pic 06 23 gr3	Saprolite		1,517		20.15	22.2	2.2	0.1930	0.0073	1.73	0.04	0.14	0.02	0.08	82.52
	Pic 06 23 gr4	Saprolite		1,517		11.04	12.1	1.2	0.1582	0.0064	2.59	0.05	0.19	0.02	0.07	88.64
	G-12-10	Saprolite	20° 06′ 42.20″S	1,533	5	16.53	18.2	1.8	0.188	0.0133	1.414	0.028	2.870	0.050	2.03	157.32
	G-12-10	Saprolite	43° 39′ 5.75″W	1,533	5	18.14	20.0	2.0	0.133	0.0058	0.877	0.026	1.985	0.048	2.26	95.58
	G-12-10	Saprolite		1,533	5	18.32	20.2	2.0	0.225	0.0080	1.626	0.041	2.691	0.064	1.65	78.41
	G-12-11_botryoidal Gt	Saprolite	20° 07′ 5.96″S	1,441	15	32.72	36.0	3.6	0.135	0.0113	0.731	0.018	0.116	0.012	0.16	184.69
	G-12-11_botryoidal Gt	Saprolite	43° 38′ 55.84″W	1,441	15	35.87	39.5	3.9	0.133	0.0140	0.660	0.016	0.082	0.009	0.12	234.42
	G-12-11_botryoidal Gt	Saprolite		1,441	15	36.72	40.4	4.0	0.133	0.0058	0.645	0.019	0.075	0.018	0.12	95.33
	G-12-11_layered Gt	Saprolite		1,441	15	28.27	31.1	3.1	0.195	0.0058	1.242	0.034	0.111	0.026	0.09	65.05
	G-12-11_layered Gt	Saprolite		1,441	15	27.35	30.1	3.0	0.191	0.0080	1.249	0.030	0.148	0.020	0.12	91.98
	G-12-12	Saprolite	20° 07′ 5.96″S	1,441	15	16.09	17.7	1.8	0.124	0.0063	1.287	0.040	0.554	0.045	0.43	40.21
	G-12-12	Saprolite	43° 38′ 55.84″W	1,441	15	28.87	31.8	3.2	0.185	0.0087	1.144	0.030	0.119	0.021	0.10	77.01
	G-12-12	Saprolite		1,441	15	22.28	24.5	2.5	0.129	0.0091	1.022	0.024	0.167	0.015	0.16	156.30
	G-12-12	Saprolite		1,441	15	26.24	28.9	2.9	0.122	0.0131	0.844	0.018	0.026	0.008	0.03	239.97
	G-12-07a	Colluvium	20° 06′ 3.07″S	1,654		0.48	0.5	0.1	0.003	0.0013	0.337	0.013	2.620	0.050	7.79	138.04
	G-12-07a	Colluvium	43° 40′ 31.82″W	1,654		1.27	1.4	0.1	0.001	0.0014	0.129	0.009	0.326	0.021	2.51	115.82
	G-12-07b (Cement)	Colluvium		1,654		0.79	0.9	0.1	0.008	0.0014	0.770	0.019	4.575	0.066	5.95	186.52
	G-12-07b (Cement)	Colluvium		1,654		0.99	1.1	0.1	0.012	0.0014	0.817	0.023	5.871	0.091	7.19	115.96
	G-12-07b (Massive)	Colluvium		1,654		7.69	8.5	0.8	0.135	0.0139	2.510	0.029	3.012	0.046	1.20	229.78
	G-12-07b (Massive)	Colluvium		1,654		20.30	22.3	2.2	0.084	0.0065	0.630	0.017	0.538	0.019	0.85	170.58
	G-12-07c	Colluvium		1,654		21.74	23.9	2.4	0.213	0.0194	1.697	0.027	0.446	0.016	0.26	202.88
	G-12-07c	Colluvium		1,654		28.86	31.8	3.2	0.205	0.0094	1.209	0.031	0.395	0.025	0.33	101.91
Serra Da Moeda	*Pic-06-25A/1*	*Duricrust*	20° 08′ 28.10″S	*1,460*	*0*	*9.2*	*10.1*	*1.0*	*0.7314*	*0.0232*	*13.32*	*0.23*	*5.49*	*0.09*	*0.41*	*89.13*
	Pic-06-25A/2	*Duricrust*	43° 58′ 35.12″W	*1,460*	*0*	*7.7*	*8.4*	*0.8*	*0.5468*	*0.0178*	*12.55*	*0.21*	*2.54*	*0.06*	*0.20*	*126.39*
	Pic-06-25A/4	*Duricrust*		*1,460*	*0*	*6.3*	*6.9*	*0.7*	*0.1988*	*0.0077*	*5.56*	*0.10*	*1.22*	*0.04*	*0.22*	*166.17*
	Pic-06-25A/5	*Duricrust*		*1,460*	*0*	*7.5*	*8.2*	*0.8*	*0.5002*	*0.0165*	*11.71*	*0.20*	*2.69*	*0.06*	*0.23*	*43.60*
	Pic-06-25A/6	*Duricrust*		*1,460*	*0*	*7.1*	*7.8*	*0.8*	*0.6373*	*0.0204*	*15.88*	*0.27*	*2.50*	*0.06*	*0.16*	*64.09*
	Pic-06-25A/8	*Duricrust*		*1,460*	*0*	*8.8*	*9.6*	*1.0*	*0.4113*	*0.0139*	*7.88*	*0.14*	*3.22*	*0.07*	*0.41*	*138.56*
	Pic-06-25B/2	*Duricrust*		*1,460*	*0*	*11.2*	*12.3*	*1.2*	*0.7130*	*0.0226*	*11.23*	*0.19*	*1.93*	*0.05*	*0.17*	*126.52*
	Pic-06-25B/4	*Duricrust*		*1,460*	*0*	*5.9*	*6.5*	*0.6*	*0.4110*	*0.0139*	*12.54*	*0.21*	*1.12*	*0.04*	*0.09*	*155.92*
	Pic-06-25C/1	*Duricrust*		*1,460*	*0*	*9.5*	*10.4*	*1.0*	*0.6144*	*0.0198*	*10.99*	*0.19*	*3.98*	*0.07*	*0.36*	*104.01*
	Pic-06-25C/2	*Duricrust*		*1,460*	*0*	*13.6*	*15.0*	*1.5*	*1.3144*	*0.0401*	*15.99*	*0.27*	*7.53*	*0.11*	*0.47*	*45.48*
	Pic-06-25C/3	*Duricrust*		*1,460*	*0*	*6.7*	*7.4*	*0.7*	*0.5642*	*0.0183*	*14.37*	*0.24*	*4.69*	*0.08*	*0.33*	*112.33*
	Pic-06-25C/4	*Duricrust*		*1,460*	*0*	*10.4*	*11.5*	*1.1*	*0.4578*	*0.0152*	*7.15*	*0.13*	*3.97*	*0.07*	*0.56*	*195.85*
	Pic-06-25C/6	*Duricrust*		*1,460*	*0*	*12.2*	*13.4*	*1.3*	*0.3409*	*0.0118*	*4.18*	*0.08*	*4.10*	*0.07*	*0.98*	*67.22*
	Pic-06-25C/7	*Duricrust*		*1,460*	*0*	*11.1*	*12.2*	*1.2*	*0.6943*	*0.0221*	*10.52*	*0.18*	*4.36*	*0.08*	*0.41*	*196.44*

Journal of Geophysical Research: Earth Surface

10.1002/2017JF004282

Table 1 *(continued)*

Site	Sample name[a]	Weathering stage	Latitute/ longitude	Elevation (m)	Depth (m)	Measured He Age (ma)	Corrected He Age (ma)[b]	±	He (nmol/g)	±	U (ppm)	±	Th (ppm)	±	Th/U	Mass (μg)
	Pic-06-26A/1	*Duricrust*	20° 05′ 9.81″S	*1,411*	*0*	*7.7*	*8.4*	*0.8*	*0.3828*	*0.0130*	*6.75*	*0.12*	*10.31*	*0.14*	*1.53*	*126.35*
	Pic-06-26A/2	*Duricrust*	43° 58′ 45.16″W	*1,411*	*0*	*2.1*	*2.3*	*0.2*	*0.0612*	*0.0037*	*4.22*	*0.08*	*4.97*	*0.08*	*1.18*	*404.08*
	Pic-06-26A/3	*Duricrust*		*1,411*	*0*	*3.8*	*4.2*	*0.4*	*0.0574*	*0.0036*	*2.26*	*0.05*	*2.16*	*0.05*	*0.96*	*256.46*
	Pic-06-26B/3	*Duricrust*		*1,411*	*0*	*1.0*	*1.1*	*0.1*	*0.0269*	*0.0027*	*2.27*	*0.05*	*10.73*	*0.14*	*4.73*	*220.37*
	Pic-06-27/4	*Duricrust*	20° 02′ 45.11″S	*1,426*	*0.5*	*1.5*	*1.7*	*0.2*	*0.0034*	*0.0020*	*0.36*	*0.01*	*0.27*	*0.03*	*0.75*	*191.78*
	Pic-06-27/5	*Duricrust*	43° 58′ 55.35″W	*1,426*	*0.5*	*1.8*	*1.9*	*0.2*	*0.0084*	*0.0021*	*0.74*	*0.02*	*0.61*	*0.04*	*0.82*	*205.45*
	Pic-06-27	Duricrust		1,426	0.5	2.0	2.2	0.2	0.011	0.0260	0.901	0.026	0.587	0.029	0.65	76.04
	Pic-06-27	Duricrust		1,426	0.5	2.8	3.1	0.3	0.025	0.0362	1.399	0.036	1.156	0.040	0.83	67.17
	Pic-06-27	Duricrust		1,426	0.5	0.4	0.4	0.0	0.002	0.0258	0.875	0.026	0.567	0.030	0.65	73.68
	Pic-06-27	Duricrust		1,426	0.5	1.5	1.7	0.2	0.010	0.0322	1.088	0.032	0.659	0.037	0.61	58.36
	SC-12-01-Dark Brown	Duricrust		1,485		27.7	30.4	3.0	0.290	0.0249	1.542	0.028	1.620	0.033	1.05	191.09
	SC-12-01_dark Brown	Duricrust		1,485		25.6	28.2	2.8	0.270	0.0187	1.559	0.031	1.609	0.036	1.03	153.77
	SC-12-04(A)	Duricrust	20° 05′ 55.45″S	1,474		8.3	9.1	0.9	0.359	0.0207	6.181	0.060	7.517	0.108	1.22	127.90
	SC-12-04(A)	Duricrust	43° 59′ 01.86″W	1,474		5.4	6.0	0.6	0.266	0.0063	3.174	0.075	24.927	0.332	7.85	51.18
	SC-12-04(A)	Duricrust		1,474		6.1	6.7	0.7	0.297	0.0089	2.783	0.062	26.434	0.322	9.50	65.78
	SC-12-04(A)	Duricrust		1,474		21.0	23.1	2.3	0.459	0.0326	2.454	0.039	6.655	0.093	2.71	158.51
	SC-12-04(B)	Duricrust		1,474		24.7	27.2	2.7	0.128	0.0102	0.558	0.016	1.681	0.035	3.01	173.79
	SC-12-04(B)	Duricrust		1,474		34.5	37.9	3.8	0.159	0.0078	0.521	0.018	1.390	0.040	2.67	104.78
	SC-12-05	Duricrust	20° 06′ 18.60″S	1,480		26.7	29.3	2.9	0.400	0.0175	1.882	0.042	3.698	0.072	1.96	97.18
	SC-12-05	Duricrust	43° 59′ 0.34″W	1,480		28.8	31.7	3.2	0.255	0.0392	1.166	0.018	1.951	0.031	1.67	342.45
	SC-12-05	Duricrust		1,480		21.5	23.7	2.4	0.594	0.0344	3.839	0.052	5.240	0.084	1.37	129.34
	SC-12-06(A)	Duricrust	20° 06′ 20.49″S	1,477		3.8	4.2	0.4	0.19	0.0042	2.77	0.06	27.03	0.33	9.77	47.67
	SC-12-06(A)	Duricrust	43° 58′ 60″W	1,477		2.7	3.0	0.3	0.26	0.0039	4.40	0.10	54.75	0.62	12.44	31.80
	SC-12-06(B)	Duricrust		1,477		23.86	26.2	2.6	1.56	0.0143	6.19	0.14	24.71	0.40	3.99	20.39
	SC-12-06(B)	Duricrust		1,477		20.18	22.2	2.2	1.19	0.0176	4.95	0.10	25.24	0.35	5.10	32.74
	SC-12-07(A)	Duricrust	20° 06′ 23.64″S	1,468		6.19	6.8	0.7	0.54	0.0196	15.88	0.06	1.04	0.03	0.07	80.36
	SC-12-07(A)	Duricrust	43° 59′ 0.57″W	1,468		7.11	7.8	0.8	0.68	0.0277	17.25	0.06	1.18	0.03	0.07	91.02
	SC-12-07B	Duricrust		1,468		21.05	23.2	2.3	0.46	0.0243	2.96	0.03	4.63	0.07	1.56	116.67
	SC-12-15	Duricrust	20° 06′ 6.12″S	1,439	-	5.53	6.1	0.6	0.47	0.0083	11.78	0.14	16.39	0.24	1.39	38.93
	SC-12-15	Duricrust	43° 59′ 01.23″W	1,439	-	5.50	6.1	0.6	0.42	0.0063	10.65	0.15	14.72	0.24	1.38	32.81
	SC-12-17(d)	Duricrust	20° 06′ 4.91″S	1,469		1.8	1.9	0.2	0.01	0.0035	0.69	0.02	2.83	0.05	4.10	117.01
	SC-12-17(d)	Duricrust	43° 59′ 1.07″W	1,469		9.0	9.9	1.0	0.08	0.0047	0.80	0.02	3.93	0.06	4.94	85.36
	SC-12-22(B)	Duricrust	20° 06′ 43.01″S	1,493		4.91	5.4	0.5	0.48	0.0053	16.31	0.21	6.69	0.16	0.41	24.21
	SC-12-22(B)	Duricrust	43° 58′ 55.72″W	1,493		3.11	3.4	0.3	0.38	0.0088	14.40	0.11	33.37	0.37	2.32	51.97
	SC-12-20(A)	Saprolite	20° 05′ 53.63″S	1,389		17.82	19.6	2.0	0.35	0.0265	3.55	0.04	0.01	0.01	0.00	170.84
	SC-12-20(A)	Saprolite	43° 58′ 49.26″W	1,389		15.97	17.6	1.8	0.30	0.0251	3.49	0.04	0.00	−0.01	0.00	183.99
	SC-12-20(A)	Saprolite		1,389		25.61	28.2	2.8	0.25	0.0227	1.79	0.03	0.01	0.01	0.00	200.50
	SC-12-20(A)	Saprolite		1,389		24.04	26.4	2.6	0.18	0.0147	1.35	0.03	0.02	0.01	0.01	181.73
	Sm-13-01	Saprolite	20° 16′ 14.55″S	1,491	2.5	27.13	29.8	3.0	0.29	0.0168	1.93	0.03	0.10	0.01	0.05	129.72
	Sm-13-01	Saprolite	43° 57′ 24.17″W	1,491	2.5	27.59	30.4	3.0	0.27	0.0116	1.78	0.04	0.11	0.02	0.06	94.80
	Sm-13-02	Saprolite	20° 16′ 14.84″S	1,493	2.5	40.05	44.1	4.4	0.125	0.0073	0.571	0.018	0.010	0.017	0.02	125.96
	Sm-13-02	Saprolite	43° 57′ 24.13″W	1,493	2.5	28.13	30.9	3.1	0.113	0.0058	0.734	0.023	0.016	0.020	0.02	107.67
	Sm-13-07	Saprolite	20° 15′ 20.4″S	1,478		26.40	29.0	2.9	0.146	0.0116	1.006	0.023	0.009	0.012	0.01	176.07
	Sm-13-07	Saprolite	43° 57′ 57.3″W	1,478		23.56	25.9	2.6	0.146	0.0117	1.126	0.024	0.018	0.012	0.02	178.21
	SC-12-16(B)_black	Rubble	20° 06′ 5.84″S	1,439		36.2	39.9	4.0	0.55	0.0391	1.87	0.02	3.94	0.05	2.11	158.05
	SC-12-16(B)_black	Rubble	43° 59′ 1.12″W	1,439		36.0	39.6	4.0	0.67	0.0149	2.42	0.05	4.25	0.08	1.76	49.28
	SC-12-16(B)_brown	Rubble		1,439		13.5	14.9	1.5	0.44	0.0159	3.47	0.05	10.72	0.13	3.09	79.77
	SC-12-16(B)_brown	Rubble		1,439		11.1	12.2	1.2	0.36	0.0159	3.29	0.04	11.07	0.13	3.37	99.27

Table 1 *(continued)*

Site	Sample name[a]	Weathering stage	Latitude/ longitude	Elevation (m)	Depth (m)	Measured He Age (ma)	Corrected He Age (ma)[b]	±	He (nmol/g)	±	U (ppm)	±	Th (ppm)	±	Th/U	Mass (μg)
	SC-12-21(A)	Colluvium	20° 06′ 19.85″S	1,470		48.54	53.4	5.3	0.08	0.0050	0.26	0.01	0.13	0.01	0.50	133.72
	SC-12-21(A)	Colluvium	43° 59′ 04.37″W	1,470		47.36	52.1	5.2	0.08	0.0059	0.19	0.01	0.45	0.01	2.42	161.86
	SC-12-21(A)	Colluvium		1,470		22.94	25.2	2.5	0.04	0.0044	0.17	0.01	0.61	0.01	3.52	227.63
	SC-12-21(B)	Colluvium		1,470		8.6	9.5	1.0	0.61	0.0414	9.83	0.03	13.57	0.13	1.38	150.83
	SC-12-21(B)	Colluvium		1,470		10.59	11.7	1.2	0.62	0.0234	8.48	0.04	9.55	0.12	1.13	84.17
	SC-12-21(D)	Colluvium		1,470		13.27	14.6	1.5	1.65	0.0417	16.35	0.09	27.53	0.32	1.68	56.46
	SC-12-21(D)	Colluvium		1,470		15.19	16.7	1.7	1.82	0.0331	11.86	0.13	43.36	0.48	3.66	40.52

[a]Samples for which blanks exceed 10% of the measured He. An error >10% was applied for those samples. [b](Italics) Data from Monteiro et al. (2014).

5. Discussion

We interpret all (U-Th)/He data in this study as precipitation ages, with age variability for a sample indicating the presence of multiple goethite generations (Monteiro et al., 2014). The relatively large sample population (291 (U-Th)/He *pAs* and 75 cosmogenic ^{3}He *aEAs*) provides a robust data set that allows addressing the histories of weathering, exposure, and erosion of the three distinct Quadrilátero Ferrífero landsurfaces (Gandarela, Moeda, and Serrinhas).

Cangas on the Gandarela plateau (Figures 1, 3a, and 5a), which are much deeper (up to 70 m) and more continuous (Baltazar et al., 2005a) than cangas on other plateaus, record significantly longer exposure (average *aEAs* = 3.5 ± 0.9 Ma, max = 5.4 ± 0.6 Ma, *n* = 24) and weathering (pAs of 53.2 to 0.8 Ma, *n* = 102) histories. Detrital grains collected on top of the Gandarela plateau, next to in situ cangas, yield *aEA* results compatible with those obtained from coexisting cangas (e.g., average = 2.8 ± 1.0 Ma, max = 4.2 ± 0.5 Ma, *n* = 11). Pebbles from creeks draining the plateau, at lower elevation sites, yield much longer *aEAs* (average = 6.2 ± 2.3 Ma, max = 10.9 ± 1.2 Ma, *n* = 9). The results suggest that, once released from the canga, hematite-magnetite clasts travel very slowly through and out of the plateau.

At Serra da Moeda, the canga blanket is thinner and discontinuous relative to Gandarela (Baltazar et al., 2005b, 2005c). The *aEAs* (average = 1.8 ± 0.3 and max = 2.0 ± 0.2 Ma, *n* = 3) and (U-Th)/He pAs (38–0.4 Ma, *n* = 48) reveal the relatively recent exposure of an old canga blanket. Detrital hematite blocks accumulated on scree wash surrounding the canga outcrops, only ~5 m topographically below the summits underlain by cangas, yield much larger *aEAs* (average = 8.6 ± 2.8 Ma, max = 10.6 ± 1.3 Ma, n = 2).

At Serra das Serrinhas, the fragmentary canga on the narrow and isolated ridges are young ((U-Th)/He *pAs* of 24.3–0.4 Ma, *n* = 78) and more recently exposed (average *aEA* = 1.8 ± 0.8 Ma, max = 3.8 ± 0.5 Ma, *n* = 13).

The cumulative concentration of cosmogenic isotopes in a canga sample probably does not record uniform exhumation, but it records a minimum exposure history as a mineral grain is uncovered and released (possibly several times) by partial mechanical breakdown of the canga, translocates back down into the profile, and eventually returns to the surface by physical erosion of the overlying material (e.g., Shuster et al., 2012). This complex history of exposure and shielding from cosmic rays suggest that our *aEAs*, which assume continuous exposure at the surface and no erosion, most likely underestimates the amount of time a sample has interacted with cosmic rays within the uppermost 2 m. Therefore, cosmogenic ^{3}He results (Table 2) suggest that the canga-covered plateaus at the QF have been exposed at the surface for at least 5.5 Ma, probably much longer.

Another important result is that cosmogenic ^{3}He concentrations for a given surface or even a single canga block may display a large range (Table 2). Two canga blocks (Figure 7) collected at slightly different elevations on the Gandarela plateau, approximately 5 km apart (Figures 1b, 3d, and 5a; Table 2), yield quite distinct ^{3}He concentrations but similar depth profiles, which suggest that the two blocks share a relatively simple history of continuous and protracted exposure at the surface. The block from the higher-elevation site (G1209) shows a longer exposure history and greater scatter in measured ^{3}He than the second block. ^{3}He scatter may reflect partial recrystallization of hematite-magnetite to goethite (Figures 4a and 4b). The coarser-grained (425–850 μm) magnetic fraction analyzed from block G1209 (Table 2) may contain a greater proportion of grains composed of mixtures of hematite-magnetite ± goethite than the finer-grained (150–425 μm) magnetic fraction analyzed for block G1201. The better-behaved ^{3}He profile for block G1201 suggests that targeting the finer-grained magnetic fraction is the most suitable approach for quantifying cosmogenic ^{3}He in Fe duricrusts.

In addition to some scatter, both vertical profiles show a slight depletion in the expected ^{3}He concentrations for the grains closest to the surface, suggesting possible ^{3}He loss by partial mineral dissolution-reprecipitation or by diffusive ^{3}He loss during bush fires. Petrographic observation and XRD analysis confirm that goethite is more abundant in the samples closest to the surface (35–45% as opposed to 25–30% in the middle of the core) and show that hydration of hematite-magnetite to goethite near the surface is partially responsible for ^{3}He loss (Figure 7). Lichens growing on the surface of canga blocks (Figures 3b–3d) facilitate weathering (Banfield et al., 1999) and near-surface water retention, driving the biogeochemical reactions that transform hematite-magnetite into goethite and partially

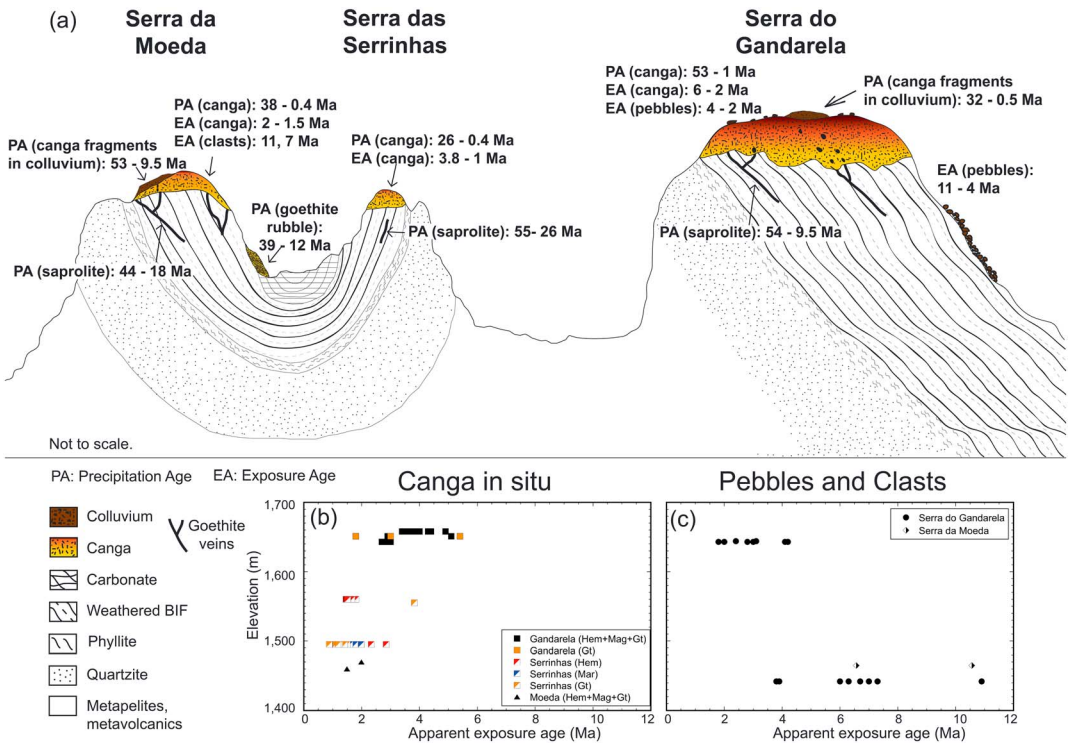

Figure 5. (a) Diagrammatic illustration of the QF landscape show that ridges and plateaus are blanketed by deeper and more continuous (Gandarela) or shallower (Moeda) and discontinuous (Serrinhas) canga blankets. Veins within saprolites and transported canga and colluvia on plateau surfaces and shoulders host some of the most ancient goethite cements dated in this study. (a, b) Apparent exposure ages (*aEAs*) measured from cosmogenic ^{3}He concentrations show that higher-elevation plateaus (Gandarela) have a longer history of exposure than lower elevation plateaus (Serrinhas and Moeda). (c) Pebbles collected on plateau summits and in streams draining the plateaus show the longest exposure histories, revealing that erosion of hematite blocks from the plateaus is a very slow process.

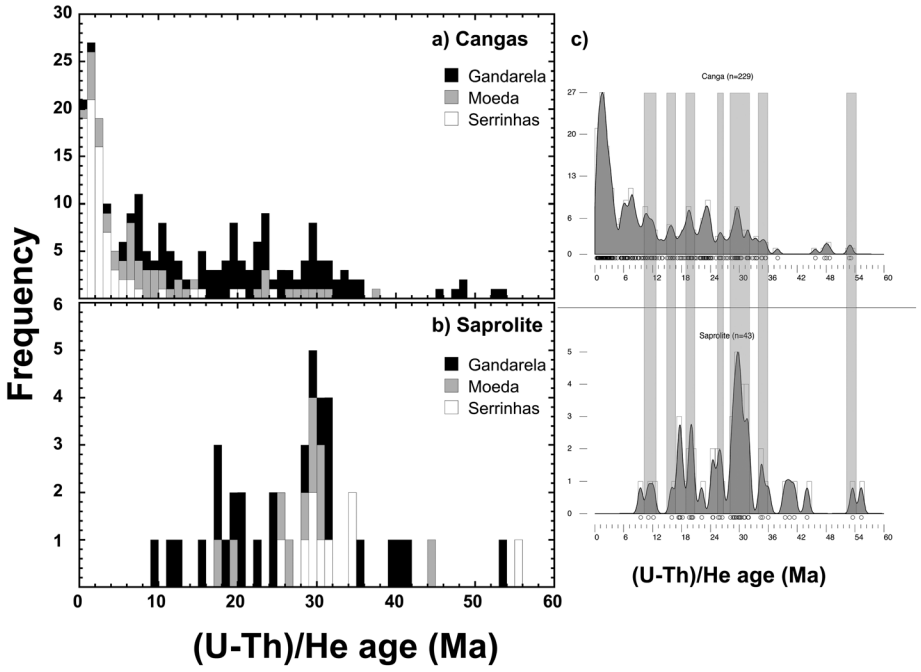

Figure 6. Histograms illustrating the frequency of goethite (U-Th)/He age distribution in (a) cangas and (b) saprolites reveal the more active and recent history of goethite cementation in cangas. The correspondence in some of the (c) major peaks in age distribution suggests that cangas and saprolites have weathered in tandem for a long time.

AGU Journal of Geophysical Research: Earth Surface

10.1002/2017JF004282

Table 2
Cosmogenic ^{3}He Analysis

Sample	Rock type	Mineralogy[a]	Location[a]	Lat./long.	Elevation (m)	Depth (cm)	Aliquot weight (mg)	^{3}He (pcc.g^{-1})	^{3}He (mat.g^{-1})	±	Production rate (at.g^{-1}.a^{-1})	Exposure age (Ma)	±	Erosion rate (m.Ma^{-1})	±	Average erosion rate (m.Ma^{-1})	Average (U-Th)/He age (Ma)	±
G1201	Canga	Hem (85%) + mag (5%) + gth (10%)	SG	20°5′ 25.39″S/ 43°41′	1,643	0		14.9	401		140	2.9	0.3	0.19	0.02	**0.20**		
G1201	Canga	Hem (85%) + mag (5%) + gth (10%)	SG	2.453″W	1,643	0.5		14.3	383		140	2.7	0.3	0.20	0.02			
G1201	Canga	Hem (85%) + mag (5%) + gth(10%)	SG		1,643	1		15.5	417		140	3.0	0.4	0.19	0.02			
G1201	Canga	Hem (85%) + mag (5%) + gth (10%)	SG		1,643	1.5		15.3	411		140	2.9	0.4	0.19	0.02			
G1201	Canga	Hem (85%) + mag (5%) + gth(10%)	SG		1,643	2		15.2	408		140	2.9	0.4	0.19	0.02			
G1201	Canga	Hem (85%) + mag (5%) + gth (10%)	SG		1,643	3		15.0	403		140	2.9	0.3	0.19	0.02			
G1201	Canga	Hem (85%) + mag (5%) + gth (10%)	SG		1,643	4		14.9	400		140	2.9	0.3	0.19	0.02			
G1201	Canga	Hem (85%) + mag (5%) + gth (10%)	SG		1,643	5		14.4	387		140	2.8	0.3	0.20	0.02			
G1201	Canga	Hem (85%) + mag (5%) + gth (10%)	SG		1,643	6		13.8	371		140	2.7	0.3	0.21	0.03			
21–2	Canga	Mag	SG	20°7′	1,651	0	21.7	25.5	686	41	134	5.1	0.6	0.11	0.01	**0.15**		
21–3	Canga	Mag	SG	5.257″S/	1,651	0	36.7	14.6	392	23	134	2.9	0.3	0.19	0.02			
21–5	Canga	Gth	SG	43°39′	1,651	0	52.3	9.9	266	16	148	1.8	0.2	0.31	0.04	**0.20**	**9.1**	**0.9**
21–5	Canga	Gth	SG	38.048″W	1,651	0	52.5	29.8	801	28	148	5.4	0.6	0.10	0.01			
21–6	Canga	Gth	SG		1,651	0	56.3	16.6	447	20	148	3.0	0.3	0.18	0.02		**24.6**	**9.0**
G1209	Hematite Block	Hem (85%) + mag (5%) + gth (10%)	SG	20°7′ 3.888″S/ 43°39′	1,658	0		19.8	532		142	3.7	0.4	0.15	0.02	**0.14**		
G1209	Hematite Block	Hem (85%) + mag (5%) + gth (10%)	SG	38.972″W	1,658	0.5		19.4	522		142	3.7	0.4	0.15	0.02			
G1209	Hematite Block	Hem (85%) + mag (5%) + gth (10%)	SG		1,658	1		18.1	486		142	3.4	0.4	0.16	0.02			
G1209	Hematite Block	Hem (85%) + mag (5%) + gth (10%)	SG		1,658	1.5		25.8	692		142	4.9	0.6	0.11	0.01			
G1209	Hematite Block		SG		1,658	2		22.5	604		142	4.3	0.5	0.13	0.02			

AGU Journal of Geophysical Research: Earth Surface

10.1002/2017JF004282

Table 2 *(continued)*

Sample	Rock type	Mineralogy[a]	Location[a]	Lat./long.	Elevation (m)	Depth (cm)	Aliquot weight (mg)	^{3}He (pcc.g^{-1})	^{3}He (mat.g^{-1})	±	Production rate (at.g^{-1}.a^{-1})	Exposure age (Ma)	±	Erosion rate (m.Ma^{-1})	±	Average erosion rate (m.Ma^{-1})	Average (U-Th)/He age (Ma)	±
		Hem (85%) + mag (5%) + gth (10%)																
G1209	Hematite Block	Hem (85%) + mag (5%) + gth (10%)	SG		1,658	2.5		22.8	613		142	4.3	0.5	0.13	0.02			
G1209	Hematite Block	Hem (85%) + mag (5%) + gth (10%)	SG		1,658	3.5		23.1	620		142	4.4	0.5	0.13	0.02			
G1209	Hematite Block	Hem (85%) + mag (5%) + gth (10%)	SG		1,658	4.5		19.9	534		142	3.8	0.5	0.15	0.02			
G1209	Hematite Block	Hem (85%) + mag (5%) + gth (10%)	SG		1,658	5.5		19.0	511		142	3.6	0.4	0.15	0.02			
G1209	Hematite Block	Hem (85%) + mag (5%) + gth (10%)	SG		1,658	6.4		21.4	574		142	4.0	0.5	0.14	0.02			
G1202 (1) r1	Pebble	Hem (90%) + mag (5%) + gth (5%)	SG	20°5′ 25.39″S/ 43°41′	1,643	0	50.6	22.1	595	2	140	4.2	0.5	0.13	0.02	**0.13**		
G1202 (1) r2	Pebble	Hem (90%) + mag (5%) + gth (5%)	SG	2.453″W	1,643	0	25.0	21.8	585	3	140	4.2	0.4	0.13	0.02			
G1202 (1) r3	Pebble	Hem (90%) + mag (5%) + gth (5%)	SG		1,643	0	25.1	21.4	576	3	140	4.1	0.4	0.14	0.02			
G1202 (2) r2	Pebble	Hem (90%) + mag (5%) + gth (5%)	SG		1,643	0	25.7	15.5	416	2	140	3.0	0.3	0.19	0.02	**0.19**		
G1202 (2) r3	Pebble	Hem (90%) + mag (5%) + gth (5%)	SG		1,643	0	25.4	14.6	392	3	140	2.8	0.3	0.20	0.02			
G1202 (3) r1	Pebble	Hem (90%) + mag (5%) + gth (5%)	SG		1,643	0	50.3	9.2	246	1	140	1.8	0.2	0.32	0.04	**0.30**		
G1202 (3) r2	Pebble	Hem (90%) + mag (5%) + gth (5%)	SG		1,643	0	25.0	9.5	254	2	140	1.8	0.2	0.31	0.04			
G1202 (3) r3	Pebble	Hem (90%) + mag (5%) + gth (5%)	SG		1,643	0	25.1	10.4	278	1	140	2.0	0.2	0.28	0.03			
G1202 (3) r4	Pebble	Hem (90%) + mag (5%) + gth (5%)	SG		1,643	0	13.6	10.3	276	1	140	2.0	0.2	0.28	0.03			
GA1302	Pebble		SG	20°5′ 36.48″S/	1,644	0	17.2	12.5	335		140	2.4	0.3	0.23	0.03	**0.21**		

Journal of Geophysical Research: Earth Surface

10.1002/2017JF004282

Table 2 *(continued)*

Sample	Rock type	Mineralogy[a]	Location[a]	Lat./long.	Elevation (m)	Depth (cm)	Aliquot weight (mg)	^{3}He (pcc.g^{-1})	^{3}He (mat.g^{-1})	±	Production rate (at.g^{-1}.a^{-1})	Exposure age (Ma)	±	Erosion rate (m.Ma^{-1})	±	Average erosion rate (m.Ma^{-1})	Average (U-Th)/He age (Ma)	±
		Hem (90%) + mag (5%) + gth (5%)		43°40′ 59.07″W														
GA1302	Pebble	Hem (90%) + mag (5%) + gth (5%)	SG		1,644	0	13.4	16.1	432		140	3.1	0.3	0.18	0.02			
GA1301 A (1) r2	Pebble	Hem (90%) + mag (5%) + gth (5%)	SG	20°7′ 06.37″S/ 43°38′	1,442	0	25.0	30.4	817	3	122	6.7	0.7	0.08	0.01	**0.08**		
GA1301 A (1) r3	Pebble	Hem (90%) + mag (5%) + gth (5%)	SG	56.64″W	1,442	0	25.6	31.5	846	4	122	7.0	0.7	0.08	0.01			
GA1301 A (1) r4	Pebble	Hem (90%) + mag (5%) + gth (5%)	SG		1,442	0	17.0	28.4	763	4	122	6.3	0.7	0.09	0.01			
GA1301 A (2) r2	Pebble	Hem (90%) + mag (5%) + gth (5%)	SG		1,442	0	25.4	27.0	727	3	122	6.0	0.6	0.09	0.01	**0.07**		
GA1301 A (2) r3	Pebble	Hem (90%) + mag (5%) + gth (5%)	SG		1,442	0	25.4	49.6	1332	6	122	10.9	1.2	0.05	0.01			
GA1301 A (2) r4	Pebble	Hem (90%) + mag (5%) + gth (5%)	SG		1,442	0	13.8	33.0	888	5	122	7.3	0.8	0.08	0.01			
GA1301 A (3) r1	Pebble	Hem (90%) + mag (5%) + gth (5%)	SG		1,442	0	52.2	17.5	472	2	122	3.9	0.4	0.14	0.02	**0.15**		
GA1301 A (3) r2	Pebble	Hem (90%) + mag (5%) + gth (5%)	SG		1,442	0	25.4	17.3	465	3	122	3.8	0.4	0.15	0.02			
GA1301 A (3) r3	Pebble	Hem (90%) + mag (5%) + gth (5%)	SG		1,442	0	25.2	17.2	461	2	122	3.8	0.4	0.15	0.02			
01A4	Canga	Gth	SS	20°15′	1,495	0	4.14	1.3	36	21	133	0.3	0.2	2.05	0.25	**2.05**	**1.2**	**1.3**
01A5	Canga	Gth	SS	23.7240″S/	1,495	0	8.96	5.6	149	31	133	1.1	0.2	0.49	0.06	**0.43**	**1.2**	**0.8**
01A5	Canga	Gth	SS	43°52′	1,495	0	16.8	7.4	198	26	133	1.5	0.2	0.37	0.04			
01A5	Canga	Hem	SS	43.8816″W	1,495	0	17.4	6.4	172	22	126	1.4	0.2	0.41	0.05	**0.41**		
01A6	Canga	Gth	SS		1,495	0	22.3	4.4	117	17	133	0.9	0.2	0.63	0.08	**0.63**	**1.6**	**1.0**
01A7	Canga	Gth	SS		1,495	0	4.28	1.1	30	21	133	0.2	0.1	2.46	0.30	**1.43**	**0.7**	**0.3**
01A7	Canga	Gth	SS		1,495	0	21.2	7.0	187	22	133	1.4	0.2	0.39	0.05			
01A7	Canga	Mt	SS		1,495	0	22.4	8.4	224	21	126	1.8	0.2	0.31	0.04	**0.31**		
01A8	Canga	Gth	SS		1,495	0	23.4	6.1	164	20	133	1.2	0.2	0.45	0.05	**0.45**	**2.1**	**1.6**
01A8	Canga	Hem	SS		1,495	0	31.3	11.0	295	20	126	2.3	0.3	0.24	0.03	**0.24**		
01A8	Canga	Mt	SS		1,495	0	37.2	7.5	201	16	126	1.6	0.2	0.35	0.04	**0.35**		
01B2	Canga	Mt	SS		1,495	0	29.4	9.3	251	21	126	2.0	0.3	0.28	0.03	**0.28**		
01B5	Canga	Gth	SS		1,495	0	8.43	1.0	26	12	133	0.2	0.1	2.82	0.34	**2.82**	**1.6**	**0.4**
01C6	Canga	Gth	SS		1,495	0	6.02	5.8	157	33	133	1.2	0.3	0.47	0.06	**0.47**	**4.9**	**2.5**

AGU Journal of Geophysical Research: Earth Surface

10.1002/2017JF004282

Table 2 *(continued)*

Sample	Rock type	Mineralogy[a]	Location[a]	Lat./long.	Elevation (m)	Depth (cm)	Aliquot weight (mg)	^{3}He (pcc.g^{-1})	^{3}He (mat.g^{-1})	±	Production rate (at.g^{-1}.a^{-1})	Exposure age (Ma)	±	Erosion rate (m.Ma^{-1})	±	Average erosion rate (m.Ma^{-1})	Average (U-Th)/He age (Ma)	±
01C6	Canga	Hem	SS		1,495	0	13.8	13.4	360	40	126	2.8	0.4	0.20	0.02	**0.20**		
08–6	Canga	Gth	SS	20°12′	1,555	0	3.06	1.3	35	25	138	0.2	0.2	2.23	0.27	**2.23**	**3.9**	**0.5**
08-9a	Canga	Gth	SS	38.0880′′S/	1,555	0	22.7	19.7	529	38	138	3.8	0.5	0.15	0.02	**1.13**	**4.1**	**1.4**
08-9b	Canga	Gth	SS	43°51′ 11.1743′′W	1,555	0	28.8	1.4	36	9	138	0.3	0.1	2.11	0.25			
Pic-06-12Ab[b]	Hematite Block	Hem	SS	20°8′ 59.28′′S/	1,560	0	20.5	7.2	193	17	132	1.5	0.2	0.38	0.05	**0.35**		
Pic-06-12Ac[b]	Hematite Block	Hem	SS	43°52′ 34.1292′′W	1,560	0	23.3	7.3	195	18	132	1.5	0.2	0.38	0.05			
Pic-06-12Ad[b]	Hematite Block	Hem	SS		1,560	0	3.8	8.9	239	42	132	1.8	0.4	0.31	0.04			
Pic-06-12Ae[b]	Hematite Block	Hem	SS		1,560	0	5.2	7.5	201	29	132	1.5	0.3	0.36	0.04			
Pic-06-12Af[b]	Hematite Block	Hem	SS		1,560	0	5.2	8.0	214	38	132	1.6	0.4	0.34	0.04			
Pic-06-12Ag[b]	Hematite Block	Hem	SS		1,560	0	27.3	8.2	220	25	132	1.7	0.3	0.33	0.04			
Pic-06-12Ba[b]	Hematite Block	Hem	SS		1,560	0	20.3	7.3	197	19	132	1.5	0.2	0.37	0.04			
Pic-06-12Bb[b]	Hematite Block	Hem	SS		1,560	0	22.8	7.5	201	16	132	1.5	0.2	0.36	0.04			
25B r3	Canga	Hem (85%) + mag (5%) + gth (10%)	SM	20°8′27′′S/ 43°58′ 35′′W	1,460	0	5.29	6.9	184	2	123	1.5	0.2	0.37	0.04	**0.37**		
SC1217 d1	Canga	Hem (90%) + mag (5%) + gth (5%)	SM	20°5′ 56.46′′S/ 43°58′	1,470	0	9.97	9.2	247		124	2.0	0.2	0.28	0.03	**0.28**		
SC1217 d2	Canga	Hem (90%) + mag (5%) + gth (5%)	SM	59.6′′W	1,470	0	10.16	9.2	247		124	2.0	0.2	0.28	0.03			
SC1218a	Clast	Hem (90%) + mag (5%) + gth (5%)	SM	20°5′ 56.46′′S/ 43°58′	1,465	0		48.6	1306		124	10.6	1.3	0.05	0.01	**0.07**		
SC1218b	Clast	Hem (90%) + mag (5%) + gth (5%)	SM	59.6′′W	1,465	0		30.2	812		124	6.6	0.8	0.08	0.01			

[a]Abbreviations: hem = hematite, mag = magnetite, gth = goethite, mt = martite, SG = Serra do Gandarela, SS = Serra das Serrinhas, SM = Serra da Moeda. [b]Shuster et al. (2012).

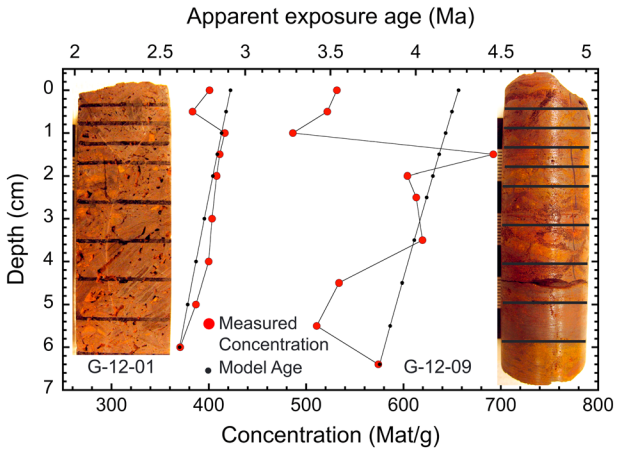

Figure 7. Cosmogenic ^{3}He and apparent exposure ages with depth for two drill cores from hematite-magnetite-rich cores in cangas reveal vertical distributions compatible with a continuous history of surface exposure (modeled results in black) for the two blocks. The scatter in the results and lower ^{3}He concentrations in the near-surface environment reveals partial ^{3}He loss during hydration of hematite-magnetite to goethite.

release cosmogenic ^{3}He. Fractures that allow the preferential penetration of weathering solutions may also lead to partial hydration of hematite–magnetite to goethite (e.g., sample G1209, Figure 7). Other factors that may account for the variability in cosmogenic ^{3}He concentrations in individual canga blocks, such as complexities of canga block geometry with respect to the surface and cosmic ray flux, or the possible rotation of the block during its weathering history, must also be considered.

It is not our intention to address each of these issues in detail here, but some sampling and analytical approaches may help to obviate some of these problems. For example, to obtain a representative exposure history for a canga plateau, we sample and analyze, by both (U-Th)/He and cosmogenic ^{3}He, as many samples as possible, of known mineralogical composition (i.e., pure hematite, magnetite, and goethite) that represent different parts of the canga (detrital blocks, cements, cemented blocks, etc.). Although more samples would be desirable, our record is comprehensive enough to reveal some of the most important aspects of the weathering and erosion histories of the QF plateaus.

5.1. The Goethite (U-Th)/He Record: Chemical Processes Controlling the Formation of Saprolites and Cangas

Weathering geochronology by (U-Th)/He analysis dates the chemical reactions and processes depicted in Figure 8 and Table 3. As summarized in those reactions, BIFs weather through mass loss during dissolution of interbedded carbonates, sulfides, silicates, and silica minerals, producing saprolites essentially composed of residual concentrations of friable and indurated hematite±magnetite (martite) ore. Alkali-earth elements and Si are leached from the system, since the reprecipitation of these elements is not energetically favored (Table 3). The scarcity of goethite suggests that iron is relatively insoluble under the conditions prevailing in saprolites, promoting the effective leaching of all other minerals and the residual concentration of hematite ± magnetite (or martite). The presence of sporadic goethite horizons or veins (Figures 3f, 5a, and 8) in saprolites suggests that soluble iron minerals (siderite or sulfides) dissolve releasing Fe^{2+}, which is then locally re-precipitated as goethite. (U-Th)/He ages for goethite veins in saprolites (Figures 3f, 5a, and 6; Table 1, e.g., SC-12-20(A)) and fragments of goethite veins in cangas (Figures 2e and 5a; Table 1, e.g., SC-12-04(B)) record, on average, older results than those obtained for goethite cement in cangas (Figures 5a and 6; Table 1). The results show that saprolites are older than the overlying cangas and suggest that cangas evolve by the slow transformation of the underlying saprolite.

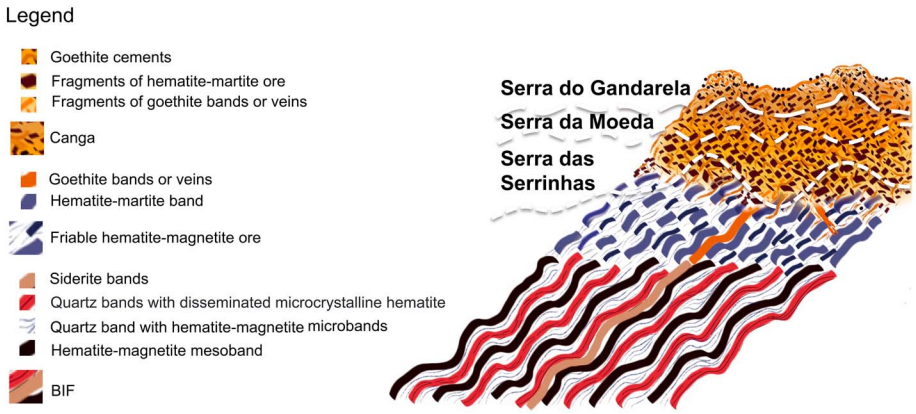

Figure 8. Diagrammatic illustration that shows the most relevant processes and reactions (Table 3) during weathering of BIF to saprolite and saprolite to canga. The dashed lines illustrate the depth of erosion recorded by the weathering profiles at Gandarela, Moeda, and Serrinhas.

Table 3
Chemical Reactions Illustrating the Most Important Processes During Weathering of BIFs

Saprolite to canga	
Reaction 1: $Fe_2O_{3(hem)} + H_2O_{(liq)} \Leftrightarrow 2\ FeOOH_{(gth)}$ (−177.6) (−56.687) 2 (−116.86)	$\Delta G = 0.567$ kcal.mol^{-1}
Reaction 2: $Fe_2O_{3(hem)} + HCOOH_{(aq)} + 4H^+ \Leftrightarrow 2\ Fe^{2+}_{(aq)} + CO_{2(aq)} + 3H_2O_{(liq)}$ (−177.6) (−82.69) (0) 2 (−18.85) (−92.26) 3 (−56.69)	$\Delta G = -39.73$ kcal.mol^{-1}
Reaction 3: $4\ Fe^{2+}_{(aq)} + O_{2(aq)} + 6H_2O_{(liq)} \Leftrightarrow 4\ FeOOH_{(gth)} + 8H^+$ 4 (−18.85) (+3.91) 6 (−56.69) 4 (−116.86) (0)	$\Delta G = -27.914$ kcal.mol^{-1}
Reaction 4: $4\ Fe_3O_{4(mag)} + O_{2(aq)} + 6\ H_2O_{(liq)} \Leftrightarrow 12\ FeOOH_{(gth)}$ 4 (−242.69) (+3.91) 6 (−56.687) 12 (−116.86)	$\Delta G = -95.348$ kcal.mol^{-1}
Reaction 5: $Al_2Si_2O_5(OH)_{4(kao)} + 5\ H_2O_{(liq)} \Leftrightarrow 2\ Al(OH)_{3(gib)} + 2\ H_4SiO_{4(aq)}$ (−906.84) 5 (−56.687) 2 (−276.1) 2 (−312.66)	$\Delta G = 12.755$ kcal.mol^{-1}
Reaction 6: $2\ H_4SiO_{4(aq)} \Leftrightarrow SiO_{2(qtz)} + 5\ H_2O_{(liq)}$ 2 (−312.66) (−204.75) 5 (−56.687)	$\Delta G = 137.135$ kcal.mol^{-1}
Banded iron formation to saprolite	
Reaction 7: $SiO_{2(qtz)} + 5\ H_2O_{(liq)} \Leftrightarrow 2\ H_4SiO_{4(aq)}$ (−204.75) 5(−56.687) 2(−312.66)	$\Delta G = -137.135$ kcal.mol^{-1}
Reaction 8: $4\ FeCO_{3(sid)} + O_{2(aq)} \Leftrightarrow 4\ FeOOH_{(gth)} + 4\ H_2CO_{3\ (aq)}$ 4 (−160.3) (+3.91) 4 (−56.687) 4 (−148.94)	$\Delta G = -425.91$ kcal.mol^{-1}
Reaction 9: $4\ Fe_5Al_2Si_3O_{10}(OH)_{8(chm)} + 5\ O_{2(aq)} + 10\ H_2O_{(liq)} \Leftrightarrow 20\ FeOOH_{(gth)} + 4\ Al_2Si_2O_5(OH)_{4(kao)} + 4\ H_4SiO_{4(aq)}$ 4 (−1801.20) 5 (+3.91) 10 (−56.687) 20 (−116.86) 4 (−906.84) 4 (−312.66)	$\Delta G = 536.92$ kcal.mol^{-1}
Reaction 10: $CaMg(CO_3)_{2(dol)} + 2\ H^+_{(liq)} \Leftrightarrow Ca^{2+}_{(aq)} + Mg^{2+}_{(aq)} + 2\ HCO^-_{3(aq)}$ (−517.1) 2 (0) (−132.30) (−108.509) 2 (−140.26)	$\Delta G = -4.229$ kcal.mol^{-1}
Reaction 11: $4\ FeS_{2(py)} + 15\ O_{2(aq)} + 10\ H_2O_{(liq)} \Leftrightarrow 4\ FeOOH_{(gth)} + 8\ HSO^-_{4(aq)} + 8\ H^+_{(aq)}$ 4 (−39) 15 (+3.91) 10 (−56.687) 4 (−116.86) 8 (−180.4) 8 (0)	$\Delta G = -1246.42$ kcal.mol^{-1}

The transformation from saprolite to canga is both chemical (quartz and carbonate dissolution and leaching) and mechanical (collapse and translocation associated with mass losses during silica and carbonate dissolution) (Figure 8). It is also strongly influenced by biological processes (Levett et al., 2016; Monteiro et al., 2014). The most important chemical processes are the dissolution and leaching of silica, carbonates, and minor sulfides, and the reductive dissolution of hematite and magnetite with subsequent precipitation of goethite. Significant mass loss during leaching of silica and carbonates creates cavities where hematite–magnetite beds, blocks, and loose grains fall and rotate, generating a collapse breccia. Sometimes these cavities are not filled, resulting in vugs, caves, and karstic pipes common in cangas (Auler et al., 2014). Direct oxidation and/or hydration of magnetite to goethite is common and energetically favored, while the direct hydration of hematite to goethite is thermodynamically inhibited (Table 3). Reductive dissolution of hematite and magnetite occurs throughout the history of canga formation, and it is aided by organic acids exuded by plants and generated by the decaying biota. Soluble iron reprecipitates locally as goethite cements (Figure 8; Table 3). Slowly, the BIF saprolite becomes devoid of silica minerals (quartz, chalcedony) and carbonates and evolves into a duricrust composed of fragments of BIF, fragments of goethite veins, blocks of hypogene hematite ± magnetite ore, and fine grains of hypogene hematite and magnetite all cemented by supergene goethite (and minor supergene hematite, gibbsite, and rarely chalcedony/opal) (Figure 8). Translocation of surface material into caves and pipes contributes to the vertical mobility of iron minerals in the weathering profile. Translocated particles may be fine grained and follow pathways created by plant roots and insect (termites, ants) burrows (Shuster et al., 2012), or, more rarely, they involve centimeter- to meter-sized blocks collapsed into caves and pipes. If erosion of the canga at the surface is slow, the canga horizon grows with time at the expense of the underlying saprolite. If erosion surpasses the rate of propagation of the canga front, cangas are slowly eroded and eventually disappear from the landscape.

(U-Th)/He results (Figures 5 and 6) reveal that the history of mineral precipitation in cangas and the underlying saprolites is roughly coeval, and some of the most frequent goethite precipitation ages (e.g.,

32–30 Ma) measured in saprolites also occur in cangas (Figure 6). The coeval events of mineral dissolution-reprecipitation in the duricrust and saprolite suggest that the saprolite-canga consortium has existed for a long time and has evolved together. Goethite precipitation events detected by geochronology are likely driven by changing climates (Carmo & Vasconcelos, 2004; Spier et al., 2006; Vasconcelos, 1999), as they are strongly dependent on an active biota at the surface to generate the organic acids necessary to promote the redox-driven dissolution-reprecipitation of iron species (Figure 8; Table 3). Peaks in the goethite (U-Th)/He record (e.g., at 32–30 Ma) likely record periods under paleoclimatic conditions conducive to weathering. The link between paleoclimate and the history of mineral precipitation in weathering profiles has been explored by several authors (e.g., Carmo & Vasconcelos, 2004; Colin et al., 2005; Hénocque et al., 1998; Vasconcelos et al., 1994, 2015), and we will not focus on this topic here.

5.2. The Cosmogenic ^{3}He Record: Mechanisms Controlling the Dismantling of Cangas

The combined *aEAs* and *pAs* reveal a dynamic history of evolution for the three profiles investigated. Gandarela, the plateau at highest elevation, most laterally extensive, and covered by the most continuous canga blanket, records the longest exposure and goethite precipitation histories (Figure 5; Table 2). Detrital material derived from erosion of this plateau suggests that slow degradation of the plateau is occurring through the breakdown of the canga and the release of hematite clasts that record an even longer ($>$ ~10.5 Ma) history of exposure (Figures 5a and 5c; Table 2). The geometry of canga blocks on the surface of the Gandarela plateau (Figures 3a–3d) hints at the likely processes leading to plateau degradation.

Typically, canga slabs protrude 20 to 50 cm from the surface and are surrounded by rills paved with detrital canga fragments and hematite–magnetite clasts (Figures 3b–3d). These geomorphic features suggest that the canga blanket undergoes slow in situ erosion by a combination of biogeochemical dissolution of goethite cements and mechanical disaggregation of the brecciated material, with local release of fragments of hematite±magnetite that slowly undergo hydration, partial dissolution, and transport toward the edges of the plateaus (Figures 2a, 3a–3d, and 5a). These clasts must be laterally transported by intermittent surface wash during major storms and must overcome barriers provided by surface protruding canga blocks. The clasts must surmount traps produced by vertical cracks in the duricrust, and they must also escape recementation. Clasts that overcome these barriers may arrive at the shoulders of the plateaus and be carried downward by diffusive processes. Ultimately, these lag fragments fall off the edges of the plateaus and supply detrital material to the shallow streams draining the plateaus or are incorporated into colluvia or transported cangas shouldering the plateaus. The old *aEA* results for the detrital blocks eroded from the plateaus ($>$10.5 Ma) confirm that dismantling, re-cementation, and ultimately erosion of cangas supplies the detritus surrounding the plateaus and that clasts released by canga fragmentation travel very slowly through and out of the system. It also suggests that the current canga blanket has slowly lost some of its upper horizons by slow chemical and physical erosion (Figures 5 and 8).

At Serra da Moeda, faster erosion of the duricrust is indicated by a thinner and discontinuous canga with younger cements ($<$38 Ma) than at Gandarela. The *aEAs* here are relatively short (~2 Ma), also suggesting a more active degradation of the duricrust and explaining the abundance of hematite detritus surrounding the exposed canga surfaces (Figures 2d and 5). A similar history of canga breakdown to that proposed for Gandarela occurs here, but the erosion history is more advanced and the current surface represents a deeper zone of a partially eroded canga (Figures 5 and 8). The abundant detrital material travels very slowly out of the system through rills (on plateau surfaces and shoulders, Figure 2a and 3a) and colluvia (on slopes and terraces, Figure 2c and 3e), as indicated by the average (8.6 ± 2.8 Ma) and maximum (10.6 ± 1.3 Ma) *aEAs* obtained for detrital hematite (Figure 5; Table 2). The even greater ages (pAs of 53 to 9 Ma) of goethite cements in detrital canga fragments from a colluvium derived from the Moeda plateau (Figures 2f and 5a) confirm the hypothesis that an older canga layer once blanketed the plateau and that this blanket has now been eroded and its detrita redeposited locally.

The lowest elevation and most discontinuous canga blanket at Serrinhas is cemented by the youngest goethites and also has a recent history of exposure (average *aEAs* ~ 2 Ma), suggesting that this plateau has been eroded to the lowest levels of the duricrust, close to the saprolite-canga interface, when compared to cangas at Moeda and Gandarela (Figures 5 and 8).

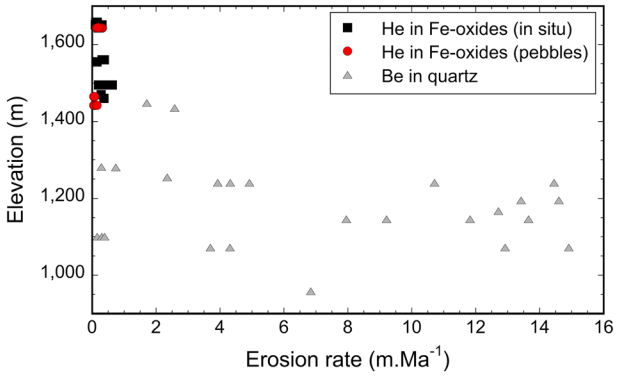

Figure 9. Erosion rates derived from in situ and detrital iron oxyhydroxides (this study) are much lower than similar rates derived from quartz (Salgado et al., 2006, 2007, 2008), consistent with the observation that the plateaus and ridges in the areas investigated are underlain by iron duricrusts overlying banded iron-formations.

5.3. Rates of Erosion for Canga Plateaus

Since we have evidence that at least some of the canga blocks have undergone a history of protracted and continuous exposure at the surface, without reburial, it is reasonable that ^{3}He concentrations in centimeter-size hematite-magnetite clasts, the mineral less likely to have undergone dissolution-reprecipitation or to have translocated up and down the profile (except where caves occur), be cast in terms of erosion rates. Calculated erosion rates are: 0.17 m.Ma^{-1} for Gandarela, 0.31 m.Ma^{-1} for Serra da Moeda, and 0.28 m.Ma^{-1} for Serra das Serrinhas. These differences suggest that erosion rates greater than ~ 0.25–0.30 m.Ma^{-1} may exceed the self-healing capacity of canga-cemented plateaus, leading to their eventual destruction (Figure 8). When a surface becomes too narrow and steep (Figures 1a, 5, and 8), running surface water and gravitational forces may drive erosion beyond the kinetic threshold of iron recementation. The eroded canga fragments may be either removed from the system or remain as detrital aprons on hill slopes (Figures 2a–2d and 5).

The erosion rates measured for cangas and detrital hematite-magnetite clasts are of similar magnitude as shorter-term rates measured from quartz sands in rivers draining quartzites in the QF (Salgado et al., 2006, 2008) (Figure 9). But at a regional scale, long-term erosion rates obtained from ^{3}He concentrations in situ and in detrital iron oxyhydroxides are much lower than erosion rates obtained from ^{10}Be in quartz (Figure 9), suggesting that plateaus blanketed by cangas are more effectively shielded from erosion than plateaus underlain by quartzites and other lithologies. This interpretation is consistent with the fact that the summits at Serras do Gandarela, Moeda, and Serrinhas are mostly underlain by BIFs and not other lithologies (Figures 1 and 5; Baltazar et al., 2005a, 2005b, 2005c).

5.4. Age Versus Elevation Relationships for Canga Plateaus

Monteiro et al. (2014) postulated that differences in (U-Th)/He ages for high- and low-elevation canga-cemented plateaus in the QF originate from two possible models of landscape evolution: (1) the QF was once equally leveled and progressively eroded forming canga plateaus at different elevations, or (2) the QF was never leveled and cangas at higher and lower elevations evolved simultaneously. Differences in erosion rates for low- and high-elevation surfaces ($<$0.17 m.Ma^{-1} for Gandarela and 0.31 m.Ma^{-1} for Moeda) if extrapolated back in time would require an unreasonable period of ~ 600 Ma for the two plateaus to share the same elevation. Therefore, the plateaus at Gandarela, Moeda, and Serrinhas probably evolved simultaneously on a landscape already showing moderate relief. More rapid physical erosion of the canga blanket as the plateaus became progressively narrower at Moeda and Serrinhas (Figure 1) likely accounts for the differences in ages, elevations, and lateral continuity for the canga blankets overlying the various plateaus.

The mechanisms envisaged for the evolution of landscapes in the QF (plateau cementation by canga, slow surface erosion, scarp retreat, etc.) implies that erosion is differential and that the relief increases with time (Vasconcelos, 1998, 1999). The narrowing of plateaus suggests that the entire landscape was once covered by a more extensive and interconnected but undulating land surface. Rounded hematite-magnetite cobbles and pebbles in colluvia and detrital cangas imply effective material transport in a mature drainage system, which is presently absent from the plateaus because of their limited catchment area. These river sediments are relics of an ancient drainage system that once existed on a now mostly eroded undulating paleo-surface that blanketed the entire region.

Despite the active histories of chemical and mechanical weathering and erosion, canga-blanketed plateaus evolve very slowly. Slow rates of erosion elsewhere are commonly attributed to rainfall deficiency in semiarid or arid conditions (Dunai et al., 2005; Nishiizumi et al., 2005; Summerfield et al., 1999). The results in this study suggest that deeply weathered BIF in tropical landscapes erode at rates equivalent to or lower than those measured in arid or semiarid environments. The joint application of ^{3}He and (U-Th)/He age measurements reveal that weathering-driven armoring of the landscape by goethite cementation and recementation in iron duricrusts offers a plausible explanation for the low rates of erosion and the preservation of continuously

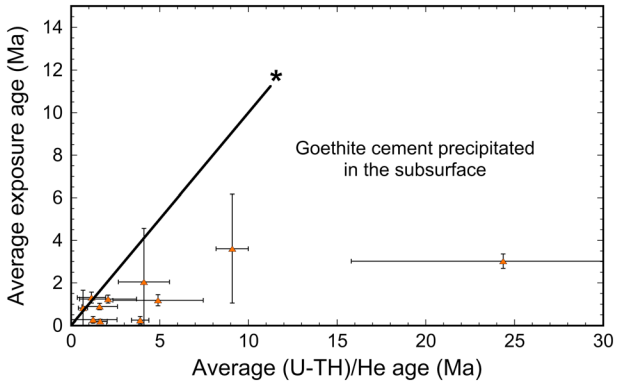

Figure 10. A correlation between goethite precipitation and exposure ages suggest that the majority of the goethite cementing cangas is precipitated and remains below the surface, suggesting that Fe cementation is primarily occurring in the subsurface, where water rich in organic acids accumulate and promote iron reductive dissolution, local transport, and reprecipitation. The 1:1 line (asterisk symbol) identifies goethite cements that precipitated and remained at the surface during their entire history.

exposed landsurfaces in tropical humid conditions. Investigating the long-term evolution of these landscapes must consider the role of weathering as an inhibitor to physical erosion, and not solely as the process that makes erodible material from bedrock.

5.5. Cangas: Self-Healing Biogeochemical Conveyor Belts

Determining both (U-Th)/He precipitation ages and ^{3}He exposure ages for the same sample permits addressing some of the complexities in a sample's history as it is exhumed through erosion. For example, exposure ages for goethite cements are either equal to or less than their precipitation ages (Figure 10), suggesting that most goethite cementation occurs in the subsurface, where the cements reside before slowly ascending to the surface. The biogenic processes interpreted to control the self-healing properties of cangas (Levett et al., 2016; Monteiro et al., 2014) may occur both at the surface and the subsurface, but a key ingredient in goethite cementation is reduced and acidic water. Since cangas are very porous and water readily infiltrates into a network of tubules, vugs, and fractures, it is likely that this infiltrating water carries organic acids leached from the surface, accumulates in subsurface void spaces, and establishes a reducing environment that can dissolve iron from hematite ± magnetite ± goethite (Figure 8; Table 3). Iron reprecipitation from these solutions may occur in the subsurface by direct oxidation of aqueous Fe^{2+} into insoluble Fe^{3+}-oxyhydroxides during the periodic influx of oxygenated meteoric waters, by neutralization of the organic acids during reaction with wall rock, or by microbially induced Fe^{2+} oxidation (Weber et al., 2006, and references therein).

The difference in (U-Th)/He *pA* and cosmogenic ^{3}He *aEA* for a fragment of goethite cement reveals how far from the surface goethite cementation may have taken place and how long it took for the cement to be brought to the surface. An alternative explanation—that cements form at the surface, translocate down into the profile, and return to the surface at a later date—is also plausible. For example, large pores, fractures, and tubules in cangas permit the downward transport of mineral grains, and geopetal textures in root and insect burrows reveal that downward translocation of mineral particles does occur. However, the translocated particles are usually small (millimeter size) and wholesale transport of large canga blocks up and down the profile, although possible where caves and karstic pipes exist, is less likely than the downward movement of weathering solutions.

Further evidence that goethite cementation takes place at depth is the presence of old goethite veins within saprolites and the extensive iron cementation that characterize the "goethite cementation-front" at the canga-saprolite interface. A strong piece of evidence for the precipitation of goethite cements at depth is provided by the (U-Th)/He goethite *pAs* from block G1209 (Figure 7). These *pAs* are ~2–4 Ma greater than the cosmogenic ^{3}He *aEAs* for the same block suggesting that goethite cementation took place at depth, below the zone of accumulation of cosmogenic ^{3}He ($<$~2 m). The 2–4 Ma difference between the goethite precipitation age and ^{3}He exposure ages reveals that it took ~2–4 Ma for a sample formed at $>$2 m depth to reach the surface, suggesting a sample exhumation rate of ~ 0.5–1 m.Ma^{-1}, compatible with the average erosion rates estimated above. The exhumation rate of ~0.5–1 m.Ma^{-1} is the net rate of transfer of friable and erodible material from the saprolite through the canga and to the drainage system. In other words, ~0.5–1 m.Ma^{-1} is the net rate of mass transfer through the canga biogeochemical conveyor belt.

6. Conclusion

The history of weathering and erosion discussed here shows that cangas are long-lasting features of BIF landscapes. The more extensive and continuous the canga cover, the more stable it is and the more effective its protective power. Similarities in apparent exposure ages (*aEAs*) for in situ canga blocks and adjacent detrital fragments suggest that cangas evolve by fragmentation and Fe recementation in situ (self-healing). Exposure ages for goethite cements are either equal to or younger than their precipitation ages, suggesting either that goethite cements formed at the surface are rapidly buried after precipitation, only returning to the surface

very slowly, or, alternatively, that most of the cementation of canga occurs in the subsurface. The difference in (U-Th)/He precipitation age (*pA)* and cosmogenic ^{3}He *aEA* for a fragment of goethite cement reveals how far from the surface goethite cementation may have taken place and how long it took for the cement to be brought to the surface. The combined ^{3}He and (U-Th)/He results suggest that biogeochemical processes interpreted to control the self-healing properties of cangas occur both at the surface but primarily at the subsurface. The history of weathering and erosion derived from the combined (U-Th)/He and cosmogenic ^{3}He records reveals that surface armoring by weathering and erosion is the primary mechanism shaping landscapes in ancient and deeply weathered BIF terrains.

The ultimate effect of canga in BIF landscapes is to provide a very stable and protracted transfer mechanism, slowly converting friable and easily erodible BIF saprolite into physically resilient goethite-cemented breccias that slowly ascend to the surface to be eventually dismantled and eroded. In that sense, cangas act as natural conveyor belts that stabilize fragments of friable weathered BIF between their breakdown at depth until their eventual delivery to the drainage system. A transfer rate of ~0.5–1 m.Ma^{-1} implies that a 70 m canga cover would need about 70–140 Ma to bring a cement formed at depth to the surface and deliver it to the drainage system. Therefore, while the role of chemical and physical weathering in BIF landscapes is to transform bedrock into material to be delivered to erosion, internal biogeochemical reactions in these systems slow this transfer down to a level where the transfer mechanism itself becomes the main force shaping the landscape.

Acknowledgments
We thank Shirley Barros, Carolina Silva, MBR and Vale for logistic support; UQ-CMM staff for help during microanalysis; and, particularly, Lindsey Hedges for help and guidance during (U-Th)/He analyses. We also thank D. Granger, A. Ault, M. Schulz, and two Editors from JGR for their constructive comments and suggestions. This project was supported by the Australian Research Council (ARC Discovery grant DP160104988) to Paulo Vasconcelos and Kenneth Farley and the Brazilian Research Council (CNPq), which sponsored Hevelyn Monteiro's PhD studies. Geochronological data set is available at http://dx.doi.org/10.1594/IEDA/100730.

References

Ab'Saber, A. N. (1966). O domínio de mares de morros no Brasil. *Geomorfologia*, *2*, 9.
Alkmim, F. F., & Marshak, S. (1998). Transamazonian orogeny in the Southern São Francisco craton region, Minas Gerais, Brazil: Evidence for Paleoproterozoic collision and collapse in the Quadrilátero Ferrífero. *Precambrian Research*, *90*, 29–58.
Alvares, C. A., Stape, J. L., Sentelhas, P. C., de M. Gonçalves, J. L., & Sparovek, G. (2013). Köppen's climate classification map for Brazil. *Meteorologische Zeitschrift*, *22*(6), 711–728.
Amidon, W. H., & Farley, K. A. (2011). Cosmogenic ^{3}He production rates in apatites, zircon and pyroxene inferred from Bonneville flood erosional surfaces. *Quaternary Geochronology*, *6*, 10–21.
Auler, A. S., Piló, L. B., Parker, C. W., Senko, J. M., Sasowsky, I. D., & Barton, H. A. (2014). Hypogene cave patterns in iron ore caves: Convergence of forms or processes? In A. Klimchouk, et al. (Eds.), *Hypogene Cave Morphologies, Selected Papers and Abstracts of the Symposium Held February 2 Through 7, San Salvador Island, Bahamas*, *Karst Water Institute Special Publication 18* (pp. 15–19). Leesburg, VA: Karst Water Institute.
Baltazar, O. F., Baars, F. J., Lobato, L. M., Reis, L. B., Achtschin, A. B., Berni, G. V., & Silveira, V. D. (2005a). Mapa geológico Gandarela na escala 1:50.000 com nota explicativa. In L. M. Lobato, et al. (Eds.), *Projeto Geologia do Quadrilátero Ferrífero - Integração e correção cartográfica em SIG com nota explicativa*. Belo Horizonte: CODEMIG.
Baltazar, O. F., Baars, F. J., Lobato, L. M., Reis, L. B., Achtschin, A. B., Berni, G. V., & Silveira, V. D. (2005b). Mapa geológico Itabirito na escala 1:50.000 com nota explicativa. In L. M. Lobato, et al. (Eds.), *Projeto Geologia do Quadrilátero Ferrífero - Integração e correção cartográfica em SIG com nota explicativa*. Belo Horizonte: CODEMIG.
Baltazar, O. F., Baars, F. J., Lobato, L. M., Reis, L. B., Achtschin, A. B., Berni, G. V., & Silveira, V. D. (2005c). Mapa geológico Casa de Pedra na escala 1:50.000 com nota explicativa. In L. M. Lobato, et al. (Eds.), *Projeto Geologia do Quadrilátero Ferrífero - Integração e correção cartográfica em SIG com nota explicativa*. Belo Horizonte: CODEMIG.
Banfield, J. F., Barker, W. W., Welch, S. A., & Taunton, A. (1999). Biological impact on mineral dissolution: Application of the lichen model to understanding mineral weathering in the rhizosphere. *Proceedings of the National Academy of Sciences of the United States of America*, *96*(7), 3404–3011.
Braun, J., Mercier, J., Guillocheau, F., & Robin, C. (2016). A simple model for regolith formation by chemical weathering. *Journal of Geophysical Research: Earth Surface*, *121*, 2140–2171. https://10.1002/2016JF003914
Carlos, D. U., Uieda, L., & Basbosa, V. C. F. (2014). Imaging iron ore from the Quadrilátero Ferrífero (Brazil) using geophysical inversion and drill hole data. *Ore Geology Reviews*, *61*, 268–285.
Carmo, I. O., & Vasconcelos, P. M. P. (2004). Geochronological evidence for pervasive Miocene weathering, Minas Gerais, Brazil. *Earth Surface Processes and Landforms*, *29*, 1303–1320.
Carmo, I. O., Vasconcelos, P. M. P., & Kohn, B. (2004). Geocronologia de intemperismo, termocronologia por traços de fissão em apatita e preservação de antigas superfícies geomorfológicas, Quadrilátero Ferrífero, SE Brasil, Congresso Brasileiro de Gelogia 42 (pp. 17–22).
Carson, M. A., & Kirkby, M. J. (1972). *Hillslope Form and Process*. Cambridge, UK: Cambridge University Press.
Chemale, F. Jr., Rosière, C. A., & Endo, I. (1994). The tectonic evolution of the Quadrilátero Ferrífero, Minas Gerais, Brazil. *Precambrian Research*, *65*, 25–54.
Colin, F., Beauvais, A., Ruffet, G., & Hénocque, O. (2005). First ^{40}Ar/^{39}Ar geochronology of lateritic manganiferous pisolites: Implications for the Paleogeone history of a West Africa landscape. *Earth and Planetary Science Letters*, *238*, 172–188.
DiBiase, R. A., Whipple, K. X., Heimsath, A. M., & Ouimet, W. B. (2010). Landscape form and millennial erosion rates in the San Gabriel Mountains, CA. *Earth and Planetary Science Letters*, *289*, 134–144.
Dorr, J. V. N. II (1969). Physiographic, stratigraphic and structural development of the Quadrilatero Ferrifero, Minas Gerais, Brazil, U.S.G.S. Prof. Paper, 614-A, Washington, DC, pp. 110.
Santos, P. A. dos (2006). Estudo de densidades de rochas e comparação de técnicas de medição, Região do Quadrilátero Ferrífero, Minas Gerais, Brasil, Dissertação de Mestrado, ISEI: pp. 58.
Dunai, T. J., López, G. A. G., & Juez-Larré, J. (2005). Oligocene-Miocene age of aridity in the Atacama Desert revealed by exposure dating of erosion-sensitive landforms. *Geology*, *33*(4), 321–324.

Fujioka, T., Fifield, L. K., Stone, J. O., Vasconcelos, P. M. P., Tims, S. G., & Chappell, J. (2010). In situ cosmogenic ^{53}Mn production rate from ancient low-denudation surface in tropic Brazil. *Nuclear Instruments and Methods in Physics Research B*, *268*, 1209–1213.

Heim, J. A., Vasconcelos, P. M. P., Farley, K. A., Shuster, D. L., & Broadbent, G. C. (2006). Dating paleochannel iron ore by (U-Th)/He analysis of supergene goethite, Hamersley Province, Australia. *Geology*, *34*, 173–176.

Hénocque, O., Ruffet, G., Colin, F., & Féraud, G. (1998). ^{40}Ar/^{39}Ar dating of West Africa lateritic cryptomelanes. *Geochimica et Cosmochimica Acta*, *62*(16), 2739–2756.

Jacobi, C. M., do Carmo, F. F., Vincent, R. C., & Stehmann, J. R. (2007). Plant communities on ironstone outcrops: A diverse and endangered Brazilian ecosystem. *Biodiversity and Conservation*, *16*, 2185–2200.

King, L. C. (1956). A geomorfologia do Brasil oriental. *Revista Brasileira de Geografia*, *2*, 147–265.

Kohn, B., Carmo, I. O., & Vasconcelos, P. M. P. (2016). Denudation history of the SE Brazil margin from combined low temperature thermochronology and ^{40}Ar/^{39}Ar weathering geochronology: Implications for landscape evolution, 15th International Conference on Thermochronology, Maresias, Brazil (pp. 88–89).

Lal, D. (1991). Cosmic ray labeling of erosion surfaces: In situ nuclide production rates and erosion models. *Earth and Planetary Science Letters*, *104*, 424–439.

Levett, A., Gagen, E., Shuster, J., Rintoul, L., Tobin, M., Vongsvivut, J., et al. (2016). Evidence of biogeochemical processes in iron duricrust formation. *Journal of South American Earth Sciences*, *71*, 131–142.

Magalhães, A. Jr., & Saadi, A. (1994). Ritmos da dinâmica fluvial Neo-Cenozóica controlados por soerguimento regional e falhamento: o vale do rio das Velhas na região de Belo Horizonte, Minas Gerais, Brasil. *Geonomos*, *2*, 42–54.

Masarik, J. (2002). Numerical simulation of in-situ production of cosmogenic nuclides. *Geochimica et Cosmochimica Acta*, *66*, A491.

Monteiro, H. S., Vasconcelos, P. M. P., Farley, K. A., Spier, C. A., & Mello, C. L. (2014). (U-Th)/He geochronology of goethite and the origin and evolution of cangas. *Geochimica et Cosmochimica Acta*, *131*, 267–289.

Nishiizumi, K., Caffee, M. W., Finkel, R. C., Brimhall, G., & Mote, T. (2005). Remnants of a fossil alluvial fan landscape of Miocene age in the Atacama Desert of northern Chile using cosmogenic nuclide exposure dating. *Earth and Planetary Science Letters*, *237*, 499–507.

Patterson, D. B., & Farley, K. A. (1998). Extraterrestrial ^{3}He in seafloor sediments: Evidence for correlated 100 kyr periodicity in the accretion rate of interplanetary dust, orbital parameters, and Quaternaty climate. *Geochimica et Cosmochimica Acta*, *62*(23/24), 3669–3682.

Salgado, A. A. R., Braucher, R., Colin, F., Nalini, H. A. Jr., Varajão, A. F. D. C., & Varajão, C. A. C. (2006). Denudation rates of the Quadrilátero Ferrífero (Minas Gerais, Brazil): Preliminary results from measurements of solute fluxes in rivers and in situ-produced cosmogenic ^{10}Be. *Journal of Geochemical Exploration*, *88*, 313–317.

Salgado, A. A. R., Braucher, R., Varajão, C. A. C., Varajão, A. F. D. C., & Nalini, H. A. Jr. (2008). Relief evolution of the Quadrilátero Ferrífero (Minas Gerais, Brazil) by means of (^{10}Be) cosmogenic nuclei. *Zeitschrift Geomophology*, *52*, 317–323.

Salgado, A. A. R., Varajão, C. A. C., Colin, F., Braucher, R., Varajão, A. F. D. C., & Nalini, H. A. Jr. (2007). Study of the erosion rates in the upper Maracujá Basin (Quadrilátero Ferrífero/MG, Brazil) by the in situ produced cosmogenic ^{10}Be method. *Earth Surface Processes and Landforms*, *32*(6), 905–911.

Shuster, D. L., Farley, K. A., Vasconcelos, P. M. P., Balco, G., Monteiro, H. S., Waltenberg, K., & Stone, J. O. (2012). Cosmogenic ^{3}He in hematite and goethite from Brazilian "canga" duricrust demonstrates the extreme stability of these surfaces. *Earth and Planetary Science Letters*, *329-330*, 41–50.

Shuster, D. L., Vasconcelos, P. M. P., Heim, J. A., & Farley, K. A. (2005). Weathering geochronology by (U-Th)/he dating of goethite. *Geochimica et Cosmochimica Acta*, *69*, 659–673.

Spier, C. A., Oliveira, S. M. B., & Rosière, C. A. (2003). Geology and geochemistry of the Águas Claras and Pico Iron Mines, Quadrilátero Ferrífero, Minas Gerais, Brazil. *Mineralium Deposita*, *38*, 751–774. https://doi.org/10.1007/s00126-003-0371-2

Spier, C. A., Oliveira, S. M. B., Rosière, C. A., & Ardisson, J. D. (2008). Mineralogy and trace-element geochemistry of the high-grade iron ores of the Águas Claras mine and comparison with the Capão Xavier and Tamanduá iron ore deposits, Quadrilátero Ferríferro, Brazil. *Mineralium Deposita*, *43*, 229–254. https://doi.org/10.1007/s00126-007-0157-z

Spier, C. A., Vasconcelos, P. M. P., & Oliveira, S. M. B. (2006). ^{40}Ar/^{39}Ar geochronological constraints on the evolution of lateritic iron deposits in the Quadrilátero Ferrífero, Minas Gerais, Brazil. *Chemical Geology*, *234*, 79–104.

Stone, J. O. (2000). Air pressure and cosmogenic isotope production. *Journal of Geophysical Research*, *105*, 23,753–723,759.

Summerfield, M. A., Stuart, F. M., Cockburn, H. A. P., Sugden, D. E., Denton, G. H., Dunai, T., & Marchant, D. R. (1999). Long-term rates of denudation in the Dry Valleys, Transantartic Mountains, southern Victoria Land, Antarctica based on in-situ-produced ^{21}Ne. *Geomorphology*, *27*, 113–129.

Tucker, G. E., & Hancock, G. R. (2010). Modelling landscape evolution. *Earth Surface Processes and Landforms*, *35*, 28–50.

Tucker, G. E., & Singerland, R. (1994). Erosional dynamics, flexural isostasy, and long-lived escarpments: A numerical modeling study. *Journal of Geophysical Research*, *99*, 12,229–12,243.

Twidale, C. R. (1956). Chronology of denudation in northwest Queensland. *Bulletin Geological Society of America*, *67*(7), 867–882.

Vance, D., Bickle, M., Ivy-Ochs, S., & Kubik, P. W. (2003). Erosion and exhumation of the Himalaya from cosmogenic isotope inventories of river sediments. *Earth and Planetary Science Letters*, *206*, 273–288.

Vasconcelos, P. M. (1998). Geochronology of weathering in the Mt Isa and Charters Towers regions, northern Queensland, Restricted Report 68R/E&M Rep. 452R, Perth, Australia, CRC LEME.

Vasconcelos, P. M. (1999). ^{40}Ar/^{39}Ar geochronology of supergene processes in ore deposits. *Economic Geology*, *12*, 73–113.

Vasconcelos, P. M. P., Reich, M., & Shuster, D. L. (2015). The paleoclimatic signatures of supergene metal deposits. *Elements*, *11*, 317–322.

Vasconcelos, P. M. P., Heim, J. A., Farley, K. A., Monteiro, H. S., & Waltenberg, K. M. (2013). ^{40}Ar/^{39}Ar and (U-Th)/He - ^{4}He/^{3}He geochronology of landscape evolution and channel iron deposit genesis at Lynn Peak, Western Australia. *Geochimica et Cosmochimica Acta*, *117*, 283–312.

Vasconcelos, P. M. P., Rene, P. R., Brimhall, G. H., & Becker, T. A. (1994). Direct dating of weathering phenomena by ^{40}Ar/^{39}Ar and K-Ar analysis of supergene K-Mn oxides. *Geochimica et Cosmochimica Acta*, *58*(6), 1635–1665.

Waltenberg K. M. (2012). Mineral physics and crystal chemistry of minerals suitable for weathering geochronology: Implications to ^{40}Ar/^{39}Ar and (U-Th)/he geochronology (PhD thesis) (421 pp.). Brisbane: The University of Queensland.

Weber, K. A., Achenback, L. A., & Coates, J. D. (2006). Microorganisms pumping iron: Anaerobic microbial iron oxidation and reduction. *Nature Reviews Microbiology*, *4*, 752–764.